13.5 Near Infrared Multiple Object Spectrograph

13.5.1 Introduction

13.5.1.1 NIRMOS Team Members

The NIRMOS (Near IR Multiple Object Spectrograph) conceptual design presented here was led by Daniel Fabricant. Edward Hertz, a mechanical engineer on the CfA staff, led the engineering studies. Henry Bergner, Warren Brown, Nelson Caldwell, Robert Fata, Thomas Gauron, John Geary, Brian McLeod, Timothy Norton, John Roll, and Andrew Szentgyorgyi all made important contributions. We thank Stephen Shectman for his contributions to the optical design of the collimator.

13.5.1.2 Science Working Group Goals for NIRMOS

The GMT Science Working Group has assembled the scientific goals for the GMT (Chapter 3) and described an initial suite of instruments (Chapter 4) that would be required to reach these goals. A capable moderate dispersion NIR spectrograph and imager has broad utility, but the Science Working Group has identified three related scientific objectives at the core of GMT's mission that define NIRMOS' ambitious specifications: (1) detection and characterization of the first galaxies, (2) assembly and mass evolution of galaxies from the early Universe to the present, and (3) chemical evolution of galaxies to z~3.5. In each of these areas, GMT is expected to break new ground with observations that are out of reach for 8 m class telescopes. The design goals for NIRMOS set forth by the Science Working Group are compared to the predicted performance for the current NIRMOS conceptual design in Table 13.5-1.

13.5.1.3 Operating Modes

13.5.1.3.1 Imaging
NIRMOS is intended to serve as a capable wide-field near-infrared imager as well as a multiple object spectrograph. NIRMOS has a straight through optical design and can be converted between an imager and a spectrograph by removing or inserting a disperser between the collimator and camera optics. In imaging mode NIRMOS offers a 7′ by 7′ field of view, using 6K by 6K of the available 6K by 10K detector array, with a sampling of 0.067″ per pixel.

13.5.1.3.2 Spectroscopy
In conventional multiple-object spectroscopy mode, a curved slit plate matching the GMT's ~2 m focal surface radius of curvature will be used as an aperture mask. At the diagonal of the ~300 mm by 420 mm (5′ by 7′) slit mask, the sag is ~15 mm. The slit mask area can be apportioned as desired: with 3″ long slitlets, up to 140 spectra can be acquired with no overlap and full spectral coverage. Using band-limiting filters, more spectra can be obtained in multiple tiers.

We have investigated Integral Field Units (IFUs) that would allow spectroscopy of a contiguous area of the sky in a single observation. We present a conceptual design for an image slicer IFU that covers an 8″ by 10″ region of the sky with 0.2″ sampling. Along the 10″ long slice, the angular resolution is set by the spectrograph. This IFU uses the entire spectrograph slit, and would be deployed in place of a slit mask.

13.5.1.3.3 Ground Layer AO Operation

A single CaF_2 element with a dichroic coating on its front surface can be inserted (with its normal tilted 30º from the optical axis) in front of the spectrograph to divert optical light to AO wave front sensors located on the instrument platform. Near-infrared light passes straight through the dichroic to NIRMOS. The rear surface of the CaF_2 dichroic element is figured to remove the aberrations introduced by this element, primarily astigmatism. The back focal distance is the same with and without the dichroic element in place, so rapid changeover between GLAO and natural seeing operation is possible. GLAO operation uses a constellation of sodium laser guide stars as discussed in the AO portion of this report.

Table 13.5-1. NIRMOS design goals compared to characteristics of this conceptual design.

Parameter	Minimum	Desired	This Design
Field Area (sq. arcmin.)	25	>50	35 for spectroscopy, 49 for imaging
Wavelength Range (μm)	1.0-2.5	0.9-2.5	0.85-2.5
Spectral Resolution	3000 with a 0.5″ wide slit	5000-10000	~3000 with a 0.5″ wide slit (~7500 with a 0.2″ wide slit), full J, H, or K coverage, and full spatial coverage. Higher dispersions possible with reduced spectral coverage.
Multiplex Advantage	100 slits 3″ long	200 slits 3″ long	7′ total slit length, corresponding to 140 slits 3″ long
Image Quality		0.15″ 80% EE diameter	0.15″ to 0.20″ 80% EE diameter
Throughput	20%	>25% peak	37%-48% imaging 28%-33% spectroscopy
Flexure	< 0.1 pixel hr-1	< 0.05 pixel hr-1	requires passive or active flexure compensation
Sampling	adequate for 0.15″ FWHM images		0.067″ pixels
Internal background	reach noise floor set by detector noise plus OH-free portions of the spectrum		Met by cooling the optics and appropriate baffles.
Special Modes	GLAO	IFU	IFU design evaluated

13.5.2   Optical Design

13.5.2.1   Detector Pixel Scale and Detector Format

The design of a spectrograph is an iterative process. However, we can illustrate the tradeoffs involved by starting with a pixel scale and field size. Let's choose the parameters that our final design uses: a pixel scale of 0.067″ per 18 μm pixel. This scale will allow us to sample the excellent 0.2″ FWHM images that GLAO may allow with 3 pixels across the FWHM. The telescope has a final focal ratio of f/8.0, and a scale of 0.983 mm arcsec^{-1}. Our final scale at the detector is 0.266 mm arcsec^{-1}, so the spectrograph camera will be operating at f/2.2. Experience with refractive IR cameras (more below on this choice) has shown that it is very difficult to design wide field IR cameras faster than f/2, so our choice of pixel scale is reasonable from this point of view as well.

If we wish to cover a 7′ by 7′ square field for imaging, we will need an array with ~6144 by 6144 pixels. To accommodate a 5′ field for spectroscopy in the wavelength direction, we need additional detector real estate because the wavelength coverage shifts as a slitlet is offset from the center of the detector in the spectral direction. We can estimate the necessary detector real estate by assuming that a dispersed spectrum in the J, H, or K band occupies 6144 pixels at R~3000. This choice at J (for example) gives a dispersion of ~0.58 Å per pixel, and R~3000 with a 0.5″ wide slit. Because NIRMOS operates near Littrow, and 7′ occupies 6144 pixels, we can accommodate 5′ of field in the spectral direction with 4400 pixels. Therefore, we need a total detector extent in the spectral direction of 4400 + 6144 pixels, or rounding to an even multiplier of 2048, 10240 pixels. We can now calculate the linear field that the spectrograph camera must address: the diagonal of a 6144 by 10240 array with 18 μm pixels, or 215 mm.

13.5.2.2   Collimated Beam Diameter

The choice of a collimated beam diameter sets the scale of the spectrograph. Since AΩ (the product of area and solid angle) is an invariant of the optical system, we can obtain the same spectral coverage with a spectrograph that has beam size β and a camera of focal length ρ covering a field angle Ω and a spectrograph with beam size 2β and a camera of focal length 2ρ covering a field angle of Ω/2.

Let's compare 300 and 150 mm beam spectrographs with the pixel scale discussed in Section 13.5.2.1. At f/8, the 300 mm beam system will have a collimator focal length of 2400 mm and a camera focal length of 648 mm; the 150 mm system will have a collimator focal length of 1200 mm and a camera focal length of 324 mm. The smaller optics sound attractive, but there are two wrinkles: (1) covering a semi-field of 107.5 mm requires that the camera accept field angles of ±18.4º and (2) gratings of twice the ruling density are required to attain the same dispersion. Both of these issues turn out to be show stoppers. We therefore decided to work out a spectrograph design with a beam diameter of 300 mm.

13.5.2.3   Refractive or Reflective Optics?

Although the initial design that we developed with a 300 mm beam used an internal focus catadioptric camera, the larger field design that we discuss here renders a catadioptric camera less attractive because a detector area of 111 by 184 mm in a 300 mm diameter beam causes vignetting losses of at least 29% before considering additional packaging and support losses.

13.5.2.4 Optics Dimensions

Simple considerations tell us that we are going to be dealing with large optics. The diagonal of a 7′ by 7′ field is 584 mm. Since the collimator has a large field lens near the telescope focus, this field lens will be ~600 mm in diameter, as will the entrance window. The field lens cannot serve as the entrance window because it is important that the slit mask be cooled. The collimator and camera elements closest to the Lyot stop are 350 mm distant, so they will have clear apertures about 300 mm + 2·350mm·tan(9.2º), or ~414 mm (9.2º is the maximum field angle). The remainder of the camera elements will have clear apertures comparable to or smaller than 414 mm. The remaining collimator elements will have dimensions comparable to or larger than 414 mm, but smaller than 600 mm.

13.5.2.5 Optical Materials

The palette of materials for refractive optics in the near infrared is limited. Calcium fluoride is the obvious material for large elements with positive power because it has low dispersion. A few optical glasses transmit well through the NIR and at least one of these, an Ohara glass, S-FTM16, works very well as a negative element in achromatizing positive calcium fluoride elements. The absorption of S-FTM16 can become significant for thick lenses at the long wavelength end of the K band. For reference, a 10 mm thick piece of S-FTM16 has an internal transmission of 0.953 at 2.4 μm. Negative elements of zinc selenide and fused quartz form less well-corrected achromatic pairs with calcium fluoride. The absorption of fused quartz is also usually a factor at the red end of the K band. Positive elements of barium fluoride are also useful in overall color correction. Many other crystals also transmit well in the infrared, but typically cannot be obtained in large sizes. One counterexample is sodium chloride, but sodium chloride has well known problems with moisture, making it a difficult choice in cryogenic optics.

The optical design that we present below uses just three materials in ten freestanding elements (including the entrance window): seven calcium fluoride elements, two S-FTM16 elements, and one barium fluoride element. The two largest calcium fluoride lens blanks that we need for the entrance window and the field lens, ~640 mm in diameter, are larger than the current production limit of ~525 mm at Saint Gobain. Saint Gobain has been contacted and is willing to modify their crystal growing equipment to produce the larger blanks that we need at a reasonable cost. Ohara has never manufactured S-FTM16 lens blanks as large as those we require for NIRMOS, but there is no known impediment to casting these blanks if the current strip casting process is converted to a pour into a single large lens mold. Ohara is currently conducting experiments to better assess the feasibility of these large blanks. The ~350 mm diameter barium fluoride lens blank is within current production capability at Saint Gobain.

The calcium fluoride entrance window has a clear aperture of 616 mm and a thickness of 75 mm. The maximum stress in this window is ~300 psi, a rather conservative number. We will investigate the expected strength of these very large calcium fluoride blanks and run careful proof tests. The consequences of a ruptured entrance window would be very serious.

13.5.2.6 Aspherics

Using aspheric elements in an optical design has typically been a wrenching decision for an optical designer because the added cost and technical risk is usually high. Aspherics are attractive because an optical design with aspherics can provide the same performance as an all-spherical design with more elements. A well-executed design with aspherics can therefore offer

higher throughput. Aspherics can be directly cut into crystalline materials by diamond turning at reasonable cost, considerably reducing their cost premium over spherical optics. Current diamond turning techniques produce surfaces of sufficient quality that no post-polishing is needed for infrared lenses. We therefore make liberal use of aspherics in the NIRMOS design.

13.5.2.7 Conceptual Optical Design

The current NIRMOS design has been refined through several stages. The four element, two aspheric collimator design is based on an initial five element all-spherical design by Steve Shectman. The five element, three aspheric camera design is based on several IR cameras designed by Steve Shectman, Harland Epps, and Daniel Fabricant.
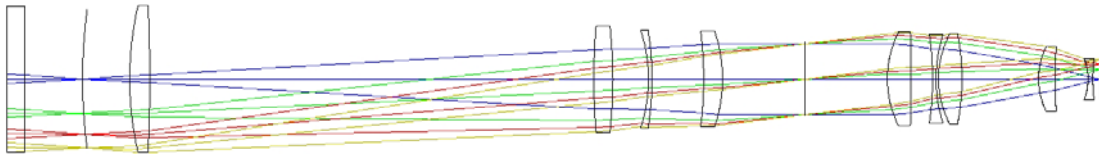
Figure 13.5-1. The NIRMOS optical layout. The 75 mm thick entrance window is at the far left, followed by the telescope focus. The camera focus is at the far right. The spacing between the last element of the collimator and the first element of the camera may be decreased when the mechanical design is more mature. There is a slight optical performance gain from decreasing this distance. The overall length of the spectrograph is 4.64 m from the entrance window to the camera focus.
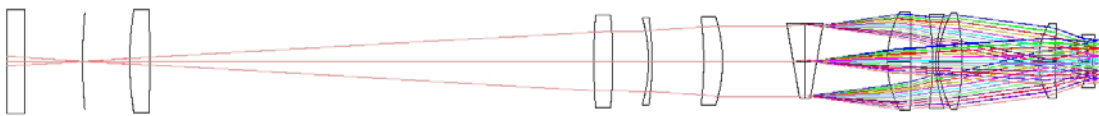

Figure 13.5-2. The NIRMOS optical layout with VPH gratings. ZnSe prisms are used to illuminate the VPH grating at the correct Bragg angle.

The optical prescription is given in Appendix A (Section 13.5.9). The image quality meets the goals set by the Science Working Group in most operating modes. Details are given in Appendix B (Section 13.5.10).

13.5.2.8 Grating Choices

13.5.2.8.1 Resolution and the OH Airglow

Martini and Depoy (2000 Proc SPIE, 4008, 695) have calculated the signal-to-noise ratio (SNR) obtained in the J and H bands as a function of spectrograph resolution and conclude that the SNR is optimized over a broad range of conditions with R~3000. Figure 13.5-3 shows the fractions of the J and H bands free of OH contamination as a function of resolution. As summarized in Table 13.5-2, NIRMOS has been designed to cover the entire J, H, or K bands at R~3000 with an 0.5″ wide slit and at R~7500 with an 0.2″ wide slit. Figure 13.5-3 shows that at R~7500, ~70% of the J and H bands are free of OH airglow.
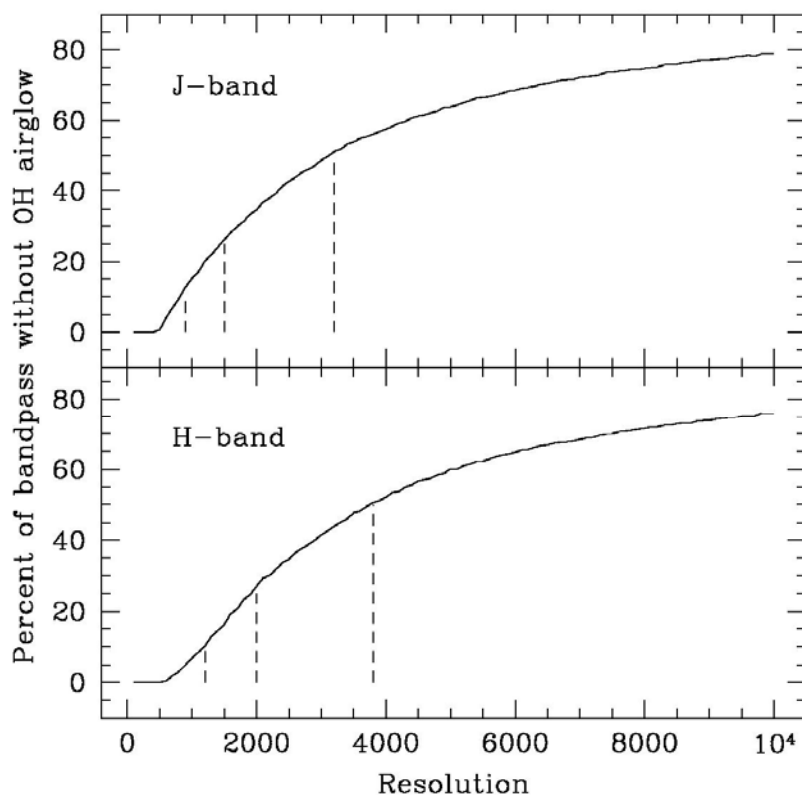
Figure 13.5-3. From Martini and Depoy's Figure 3. The fraction of pixels in the J and H bands free of OH contamination as a function of resolution. The dashed lines mark the resolutions where 10%, 25%, and 50% of the pixels are free of OH airglow. (R=900, 1500, an 3200 for J, and R=1200, 2000, and 3800 for H.

13.5.2.8.2 Introduction to Grating Choices

The GMT NIRMOS is designed to use transmission gratings principally because it is difficult to mask the rotating pupil image of the GMT projected anamorphically onto a reflection grating operating off Littrow. If we instead attempt to mask a pupil image formed well ahead of the grating and clear of the diffracted beam, the size of the reflection grating grows unacceptably. There are two choices for transmission gratings: conventional grisms using surface relief gratings and Volume Phase Holographic (VPH) gratings. Surface relief gratings are a well developed

technology, but high dispersion surface relief gratings are not efficient because the required steep facet angles lead to total internal reflection losses. VPH gratings offer potentially higher dispersion, but lose efficiency in wide field applications. VPH gratings for low dispersion applications are difficult to make since the required grating thicknesses are difficult to manufacture, and the thicker gratings have larger losses for off-axis illumination.

13.5.2.8.3   VPH Gratings

A few equations describe the approximate performance of VPH gratings. (A nice review is found in Barden et al., 2004 PASP, 112, 809.) The peak diffraction efficiency is achieved when:

$$\Delta n_g\, d \approx \lambda/2$$

Note that Δn_g is the refractive index modulation in the VPH grating; the typical maximum index modulation is ~0.105. The parameter d is the grating depth, typically 10 to 20 μm.

The Bragg condition defines the spectrograph geometry where VPH gratings offer their peak performance:

$$m\, \nu\, \lambda = 2 \sin(\alpha)$$

Here, m is the order, ν is the grating groove frequency, λ is the wavelength of interest, and α is the angle of incidence in air.
The efficiency falls to 50% of the peak diffraction efficiency at an incidence angle that deviates from the Bragg condition:

$$\alpha_{50} \approx 1/(2\, \nu\, d)$$

Note that as the ruling density and the grating thickness increase, the grating efficiency for large incidence angles decreases.

An approximate formula for the bandwidth where the diffraction efficiency falls to 50% of the peak diffraction efficiency is:

$$\Delta\lambda_{50} \approx (\lambda_{Bragg} \cot(\alpha_g))/(\nu\, d)$$

Here α_g is the angle of incidence in the VPH DCG material. The average bulk index of the Wasatch Photonics DCG material is 1.3. Therefore:

$$\alpha_g = \arcsin((\sin(\alpha))/1.3)$$

VPH grating properties for a range of gratings operating with a 2450 mm focal collimator, 648 mm focal length camera, 6144 by 10240 pixel detector array, and 0.5″ slit width are shown in Table 13.5-2. **Gsolver** was used to calculate the grating efficiencies in Table 13.5-2 and Table 13.5-3. The parameter α_{50} gives the approximate off-axis angle at the telescope focus where the diffraction efficiency drops to 50% of the peak. The diffraction efficiencies in first order do not include substrate reflection losses, manufacturing tolerances, and DCG or epoxy absorption, but give the full range of efficiencies in the indicated band. The "spec offset" column gives the maximum off-axis angle at the telescope focal plane for full spectral coverage.

Table 13.5-2. VPH Grating efficiencies.

Band	ν lpm	Res R 0.5″ slit	Res R 0.2″ slit	Diffraction Efficiency	Δn_g	d (μm)	inc angle	α_{50}	spec offset for full spec coverage
JH	200	1424	3560	0.44-0.86*	0.0300	23.3	8.05º	4.4′	±2.4′
HK	160	1549	3872	0.47-0.87[#]	0.0400	23.8	8.74º	5.4′	±2.4′
J	450	2825	7062	0.76-0.95	0.0600	10.0	15.66º	4.5′	±1.9′
H	360	3030	7574	0.82-0.95	0.0600	13.3	16.74º	4.3′	±2.6′
K	255	3017	7542	0.82-0.92	0.1050	11	16.67º	7.3′	±3.0′

* Diffraction efficiency >70% from 1.15 to 1.8 μm.
[#] Diffraction efficiency >70% from 1.63 to 2.4 μm.
Higher dispersion gratings with reduced spectral coverage can be provided.

The JH and HK gratings are probably better implemented with conventional surface relief grating technology as shown in Table 13.5-3.

Table 13.5-3. Surface relief grating efficiencies.

Band	ν lpm	Res R 0.5″ slit	Res R 0.2″ slit	Diff Effic	grism angle	spec offset for full spec coverage
JH	175	1400	3500	0.58-0.77	28.2º	±2.5′
HK	130	1431	3577	0.60-0.77	29.6º	±2.7′

The grating efficiencies as a function of wavelength are given in Appendix C (Section 13.5.11).

13.5.2.9 Throughput

For a refractive spectrograph covering a wide field of view, NIRMOS has relatively few elements. Unfortunately, all of these elements must be freestanding because bonded, greased, or oiled interfaces are not compatible with a cryogenic environment. Each lens surface will require an effective antireflection coating covering the range 0.85 to 2.5 μm.

We begin by estimating the average throughput for imaging in Table 13.5-4.

Table 13.5-4. Estimated imaging throughput.

Band	Hawaii-2RG efficiency	20 glass-air surfaces	Filter	Optics Transmission	Telescope (2 Al surfaces)	Throughput NIRMOS+GMT
Z	0.66	0.80	0.85	0.98	0.83	0.37
J	0.71	0.80	0.85	0.98	0.87	0.41
H	0.78	0.80	0.85	0.98	0.92	0.48
K	0.84	0.80	0.85	0.87	0.96	0.48

The average throughput for spectroscopy in these bands is reduced by the reflectivity losses at the bending prisms and by the efficiency of the gratings. The average throughput for spectroscopy with VPH gratings is estimated in Table 13.5-5.

Table 13.5-5. Estimated spectroscopy throughput.

Band	Imaging Throughput	VPH grating average efficiency	Prism reflectivity losses	Final Spectroscopic Throughput
J	0.41	0.75	0.92	0.28
H	0.48	0.75	0.92	0.33
K	0.48	0.70	0.92	0.31

13.5.3   Integral Field Unit

13.5.3.1   Introduction

Many astronomical observations can benefit from spatially resolved spectroscopy over a two-dimensional field on the sky provided by an Integral Field Unit (IFU). An IFU for NIRMOS should take advantage of the high spatial resolution expected during periods of excellent seeing and with GLAO operation, provide high throughput at wavelengths between 0.85 and 2.5 μm, and take advantage of NIRMOS's large 6K by 10K detector array. The IFU must remap its 2D input area to a single 7′ long slit at its output. Placing a reimager in front of the IFU allows us control the focal plane scale at the IFU and allows us to place a clean, cold pupil before the focal plane that is not distorted by diffraction effects. We consider lenslet, optical fiber, and image slicer IFU designs, and then present a design for an imager slicer IFU, which appears to be the best choice.
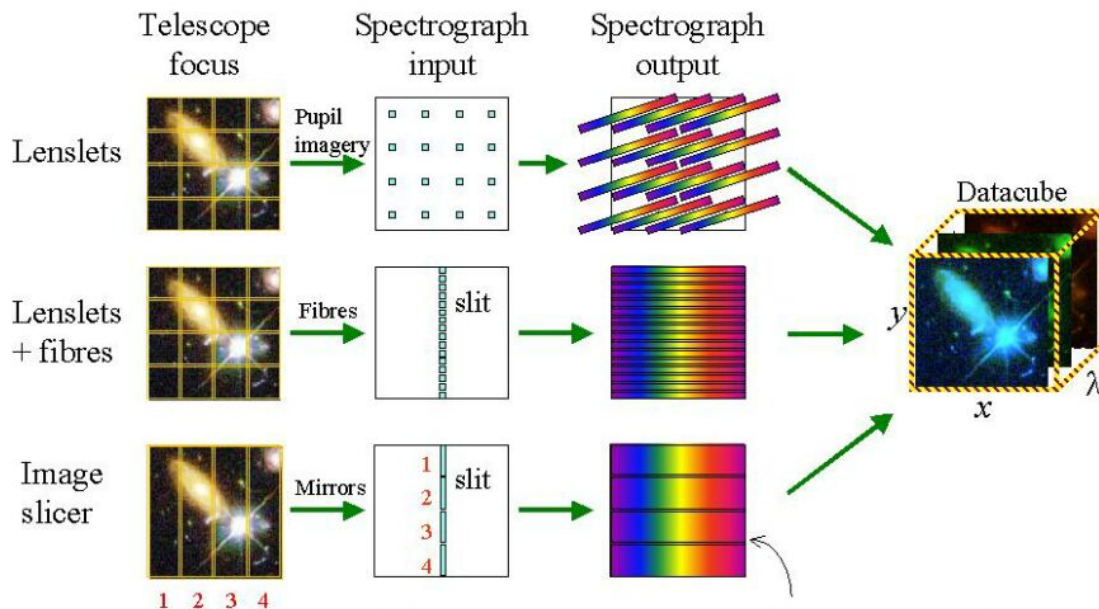
Figure 13.5-4. Three different techniques used to make an IFU: lenslet arrays, fiber optics, and image slicer mirrors. (Astronomical Instrumentation Group, University of Durham).

13.5.3.2   IFU parameters

We begin by choosing the appropriate spatial scale to sample. Because the total number of spatial elements is limited by the detector area, the spatial scale we chose also sets the IFU's field of view. Point sources benefit from spatial sampling near the expected telescope PSF, but extended sources may benefit from coarser sampling if we aim to detect low surface brightness objects against the sky background and read noise. Given NIRMOS's emphasis on wide field spectroscopy, it may be more interesting to sample a larger area with greater sensitivity, and leave very fine spatial sampling to an IFU in a diffraction limited AO instrument. Therefore, for this design study, we adopt 0.2″ spatial sampling. Assuming that the IFU arranges the light onto a single slit 420″ long, 0.2″ spatial sampling allows 2100 resolution elements, giving the IFU an ~8″ x 10″ field of view.

13.5.3.3   Reimager

Depending on the style of IFU (lenslet array, fibers, or slicer) and the desired spatial sampling, an IFU will have to be fed at focal ratios ranging from f/30 to f/300. This requires a re-imager in front the IFU. We can use the re-imager to place a cold pupil ahead of the IFU. Because of space constraints, the collimated beam diameter of the re-imager should be as small as possible, but not so small that a cold pupil mask suffers from excessive diffraction. In practice, we found a 20 mm diameter cold pupil to be as small as we could push the optical design. For a 1:6 re-imager producing an f/48 beam, a 20 mm diameter pupil requires a 1 meter focal length.

We considered refractive, two-mirror, and Offner-inspired three-mirror designs for the reimager. The refractive and three-mirror reimagers produce excellent images, but we present the three-mirror design here because it minimizes the part count. The adopted 1:6 re-imager is shown in Figure **13.5-5** and produces diffraction limited images.
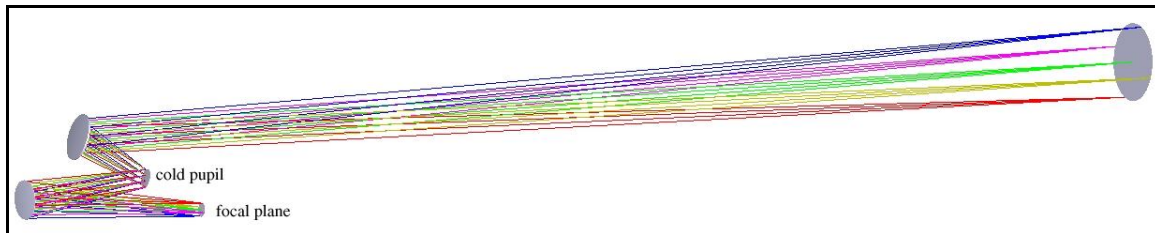

Figure 13.5-5. Offner-inspired 1:6 re-imager. The final mirror is an off-axis parabola; the other two are spheres.

13.5.3.4   Choosing an IFU Design

13.5.3.4.1   Lenslet IFU

A lenslet array is the simplest and potentially highest-throughput IFU design. A lenslet array accepts the light from the reimager foreoptics and converts it to the focal ratio expected by the spectrograph (f/8 in our case). In practice, the lenslet array is rotated so that the spectra from a row of lenslets do not overlap. Figure 13.5-6 shows the Keck OSIRIS IFU.
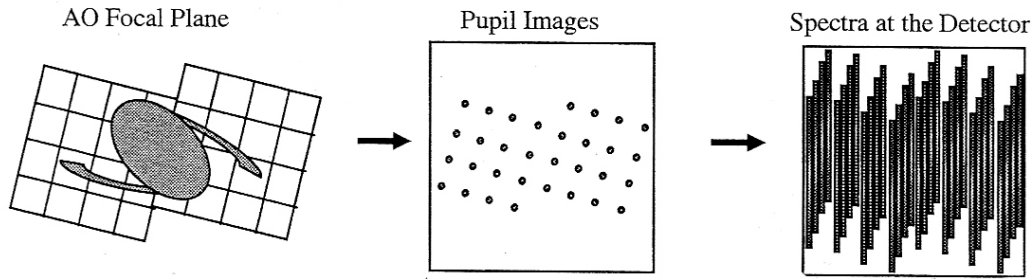
Figure 13.5-6. Cartoon of a lenslet IFU design (Larkin et al. 2003 Proc SPIE, 4841, 1600).

This approach is not well suited to large focal planes, since the size of the lenslet array is approximately the size of the slit mask used for conventional multiobject spectroscopy (300 by 420 mm). We then need to map 8″ by 10″ onto this huge scale and the reimaging optics become impractically large.

13.5.3.4.2 Fiber IFU

A fiber based IFU gives a lot more flexibility than a pure lenslet design. The simplest fiber IFU design is a bare fiber bundle. If the fiber bundle is placed at the f/8 focal plane, then 200 μm core fiber will sample at 0.2" resolution. However, because 25 μm cladding is needed at near-IR wavelengths, the filling factor of a 200/250 core/clad fiber bundle is only 58%.

To achieve a nearly 100% filling factor across a patch of sky, a fiber IFU must be fed by a lenslet array. A fiber + lenslet design also allows us to feed the fibers at faster focal ratio, and then convert it back to f/8 with an output lenslet array. A sketch of a fiber + lenslet design is shown in **Figure 13.5-7**.
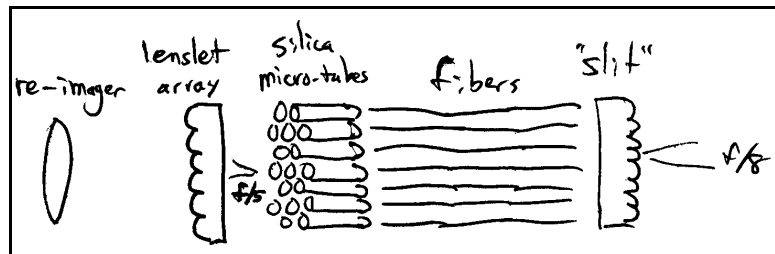

Figure 13.5-7. Sketch of fiber + lenslet IFU.

Unfortunately, a throughput estimate of the fiber + lenslet design is not promising. Assuming that the back sides of the lenslet arrays can be antireflection coated, there are a total of 4 uncoated and 2 AR-coated surfaces yielding a transmission of 82%. Lenslet arrays are not perfect devices: scattering from edges and surface roughness of the lenslet surfaces will lose an additional ~5% per lenslet array. Finally, misalignment of light onto the fibers, and focal ratio degradation in the fibers, will result in additional losses of ~5%. Assuming that we use ZrF fiber with near perfect internal transmission, the fiber + lenslet design will have a throughput of 70% at best. This poor throughput estimate suggests that an all-reflective image slicer may be the best approach. The throughput of reflective image slicers has been measured at 80 to 90%.

13.5.3.4.3 Baseline Image Slicer IFU

The image slicer design adopted here is based on the Advanced Image Slicer (AIS) concept (Content et al. 1997 Proc SPIE, 2871, 1295). The image slicer consists of three optical

components: a stack of slicer mirrors, an arc of "pupil" mirrors, and an arc of "slit" mirrors. The AIS concept gives power to the slicer mirrors so that pupils are formed on the beam-steering pupil mirrors. Because we are re-imaging the slices onto a very long 420 mm slit, we have to confront large off-axis angles. We find that the pupils become too far off-axis (>30º) and have unacceptable off-axis aberrations for input beams faster than f/48. However, slower input beams result in physically large systems, which are also undesirable. For the optical design presented here, we use the f/48 Offner-inspired 1:6 re-imager (**Figure 13.5-5**). The physical scale of the slicer mirror is thus forty 1.2 mm x 60 mm mirrors (each sampling 0.2″ x 10″).
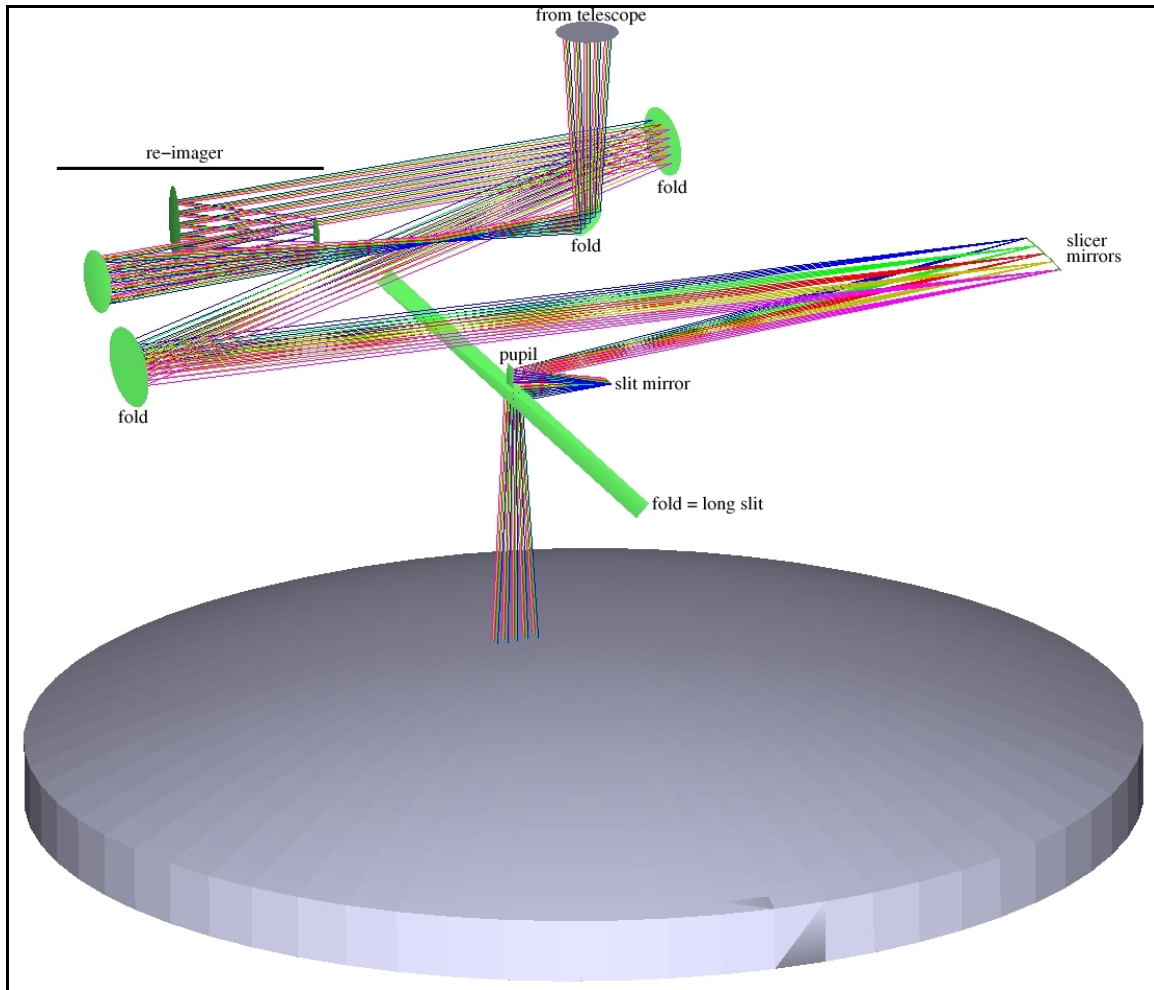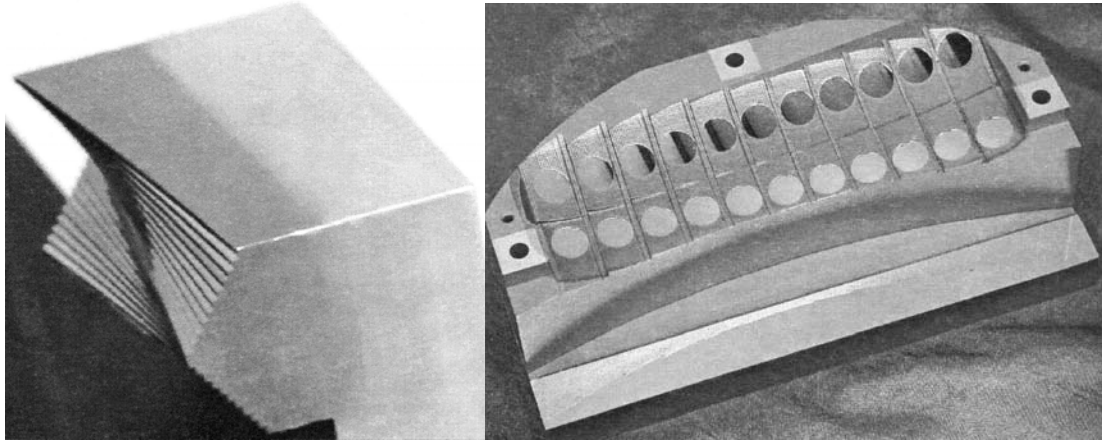

Figure 13.5-8. Our image slicer design, showing rays from the on-axis slice. Light from the telescope hits a fold mirror, goes through a three element re-imager, and is folded twice. The IFU consists of a stack of slicer mirrors, an arc of "pupil" mirrors, an arc of "slit" mirrors, and finally a fold mirror to send the light into the spectrograph. The first spectrograph lens is shown at the bottom for scale.

Our optical design is shown in **Figure 13.5-8** for a single, on-axis slice. In **Figure 13.5-8**, light from the telescope comes from the top and encounters a fold mirror 90 mm above the focal plane. The light is then sent into the three-element re-imager (**Figure 13.5-5**). The resulting f/48 beam is then folded by two mirrors before encountering the stack of image slicer mirrors on the far right. The slicer mirrors break the field into forty slices and send each slice to its own pupil mirror. The

pupil mirrors have power and reimage the light onto the "slit" mirrors, so that the light enters the spectrograph at f/8. The long slit is formed by a final long, thin fold mirror, which sends the light into the spectrograph.

Figure **13.5-9** shows the slicer mirrors and pupil mirrors of the FISICA IFU (Glenn et al. 2004 Proc SPIE, 5492, 1264). Both pieces are diamond turned from monolithic pieces of aluminum, which allows tight control of the relative alignment of each optical surface. The FISICA design uses two lines of pupil mirrors to reduce the off-axis angles coming from the slicer, a feature not currently a part of our baseline design.

Figure 13.5-9. A typical slicer mirror and a pupil mirror, used in the FISICA near-IR IFU (Glenn et al. 2004).

We asked Robert Content, the originator of this image slicer concept, to review our image slicer design and to suggest improvements. His major suggestion was to allow the radii of curvature of the slicer mirrors to vary. The telescope focal surface is curved, and each slice must be positioned correspondingly at the spectrograph's entrance slit. This constraint means the pupil mirrors want to be at different distances from the slicing mirror, which in turn forces the slicer radius of curvature to change from slice to slice so that the pupil is properly focused on the pupil mirrors. As a result of this change, the aberrations of our original image slicer design were reduced and the long slit correctly follows the radius of curvature of the focal plane.

Content states that the remaining major problem with this optical design is the large off-axis angles of the pupil mirrors. One solution is to use two lines of pupil mirrors instead of one. This change allows the pupil mirrors to be placed twice as far from the slicer mirrors, thus reducing the maximum off-axis angle. Another solution is to increase the magnification onto the IFU, though this increases the size of the system.

The optical design presented here fits into a cylindrical volume 150 mm high and 600 mm in diameter. The IFU is too large to fit into a single slit mask cartridge, but could take the place of an entire slit mask cassette. The IFU could then use existing mechanisms to slide in and out of the optical path. The IFU contains a single moving part: the cold pupil mask in the reimager optics must rotate to match the telescope pupil. All the other optical components of the IFU are fixed and aligned to each other. The most important alignment tolerance will be making sure the IFU is orientated at the correct angle with respect to the spectrograph, to avoid light loss inside the spectrograph. This image slicer is a viable design but it must be developed further. Fully

modeling all 40 slices will require additional work. Using a double row of pupil mirrors will complicate the packing and likely require a different folding arrangement.

13.5.4   Mechanical Design

13.5.4.1   Cryogenic Requirements and Thermal Background

The operating temperature of the spectrograph is set by the requirement that the background due to thermal emission from the optics be significantly below the darkest part of the night sky spectrum. We take our estimate of the night sky brightness from Maihara et al. (1993 PASP, 105, 940) who quote a sky brightness of 590 photons/s/m^2/arcsec^2/μm between the OH lines in the H-band. We assume a worst-case resolution of 10000 and a slit width of 0.5", and a throughput of 0.5 excluding the detector. This measurement should be viewed as an upper limit to the true between-the-line flux, as Maihara et al. do not consider the contribution of ghosts and scattering. We intend to undertake a more thorough investigation of the flux between the lines as a function of wavelength.

For this calculation we assume that the detector is immersed in a blackbody radiation field of 2π steradians and unity emissivity. This is only slightly pessimistic, as most of the solid angle seen by the detector will be the baffle tubes surrounding the lenses. We assume that the detector has a 2.6 μm cutoff.   The cutoff wavelength is a critical parameter in determining the optics temperature. The results of integrating the blackbody function are shown in Figure 13.5-10.   An optics temperature of 125 K will give a healthy margin of 1000 between the blackbody flux and the sky flux.
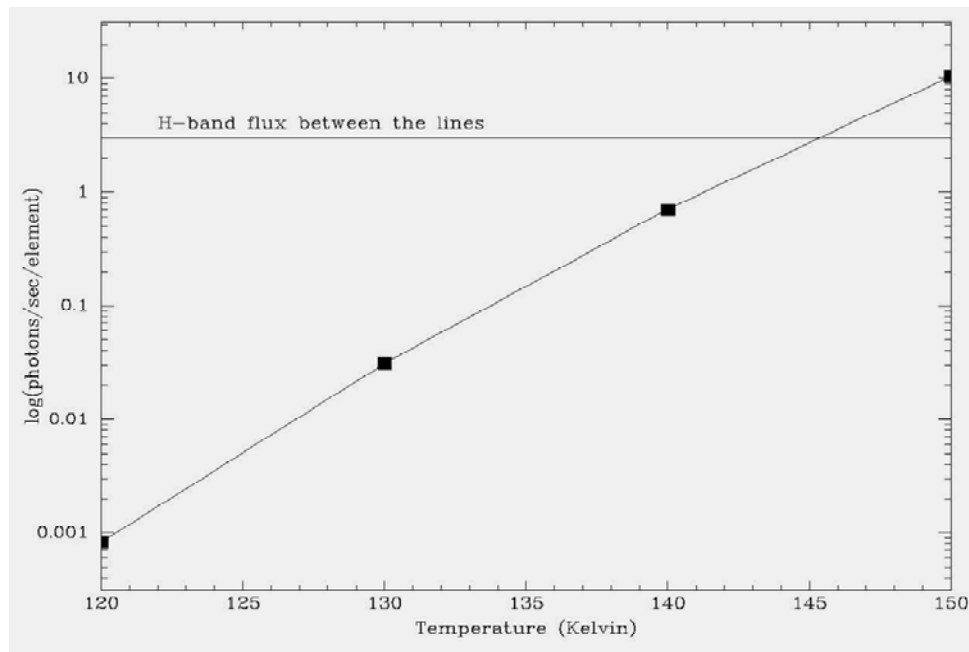

Figure 13.5-10. Background vs. optics temperature.

The slit mask and optics in front of the filter and Lyot stop can be slightly warmer because the filters will reject radiation outside of their bandpasses. The worst case we've considered here is where the blue-end of the K-band will be affected by thermal emission coming through the K

13.5-14

filter. A conservative calculation indicates that the slit mask and collimator optics temperature can be as high as 135 K.

A cold pupil stop shaped to match the GMT's seven-segment pupil will be used to reject thermal radiation from the telescope structure and as a sky baffle. This pupil stop must rotate to compensate for the rotation of the instrument rotator, and to remain fixed with respect to the primary mirrors. The IFU will contain a similar rotating pupil stop to perform the same function, unaffected by the diffraction introduced by the image slicing optics.

13.5.4.2   Gregorian Instrument Volume and Weight Limits

NIRMOS will be deployed at the straight Gregorian focus of the Giant Magellan Telescope. It will be mounted to the Instrument Rotator on the telescope Instrument Platform as shown in Figure 13.5-11. The total weight limit for the Gregorian instruments is 50,000 pounds. The Gregorian instrument volume is a cylinder of 6.35 m diameter and 7.6 m long. The NIRMOS conceptual design described in this document reaches the full weight limit of 50,000 pounds, uses the full 6.35 m diameter, but only 5.5 m of the allowed 7.36 m cylinder length.
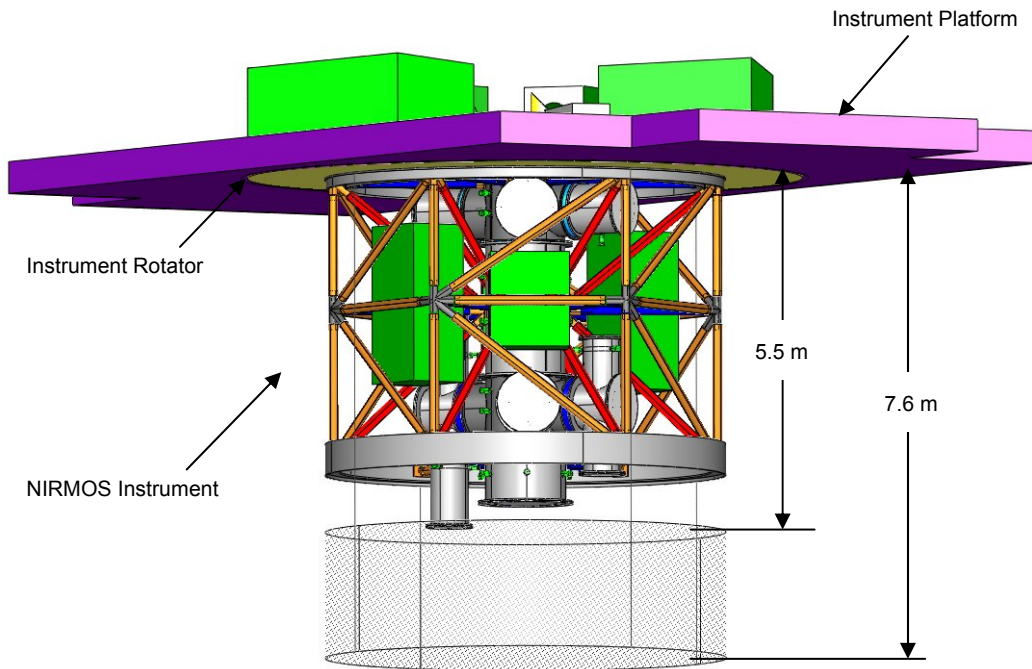

Figure 13.5-11. Gregorian Instrument Volume

13.5.4.3   NIRMOS Instrument Mechanical Concept

NIRMOS uses a modular vacuum vessel to provide a cryogenic environment for the cooled optics. Similar cassette-type mechanisms are used to exchange slits, filters, pupil masks, and disperser elements. Mechanism modules are located in independently cooled housings that may be sealed off from the main instrument housing with gate valves during maintenance and/or device exchange. The gate valves have rectangular openings at most 650 mm long and 250 mm high.

The NIRMOS thermal system will maintain the temperature of the optical elements at ~100 K and the detector at 70 K. Cryocoolers will be distributed along the chamber walls of the instrument package. The cryocoolers are mounted to the outer wall of the vacuum chamber sections with their cold heads passing through the radiation shield. Temperature sensors allow the cryocooler controllers to maintain components at the desired temperature and to ensure appropriate cooling and warm-up times.

The conceptual design includes two sets of 8 slit masks in independent assemblies. Individual slit masks or sets of eight may be exchanged during the daytime. Either set of eight slit masks may be replaced with an Integral Field Unit Assembly (IFU). Space for twelve filters and three pupil masks is included. NIRMOS will provide for five volume-phase holographic (VPH) gratings and three surface relief grisms for lower dispersions.
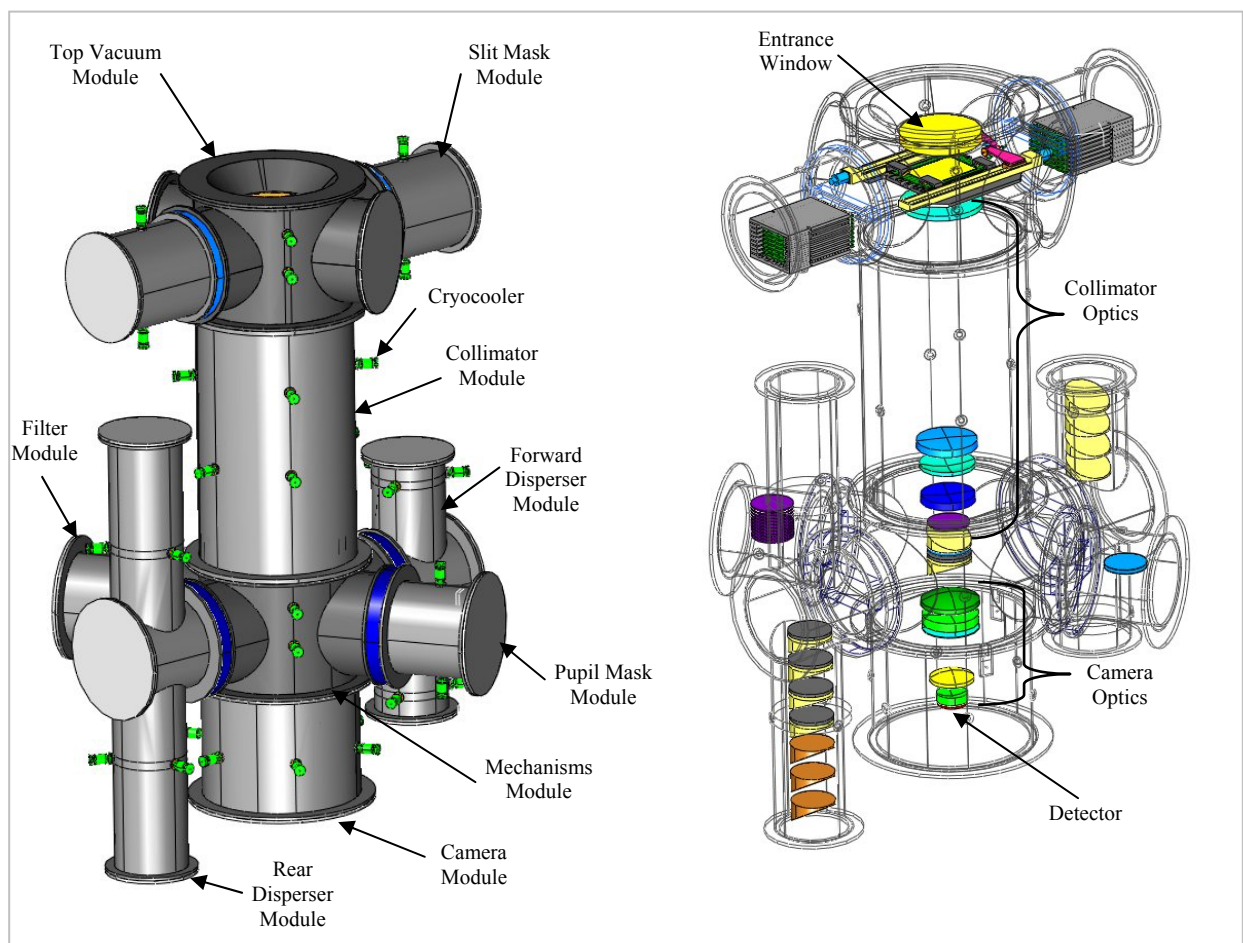
Figure 13.5-12. Layout of Vacuum Vessel and Major Assemblies. The gate valves (shown in blue on the left) have rectangular openings at most 650 mm long and 250 mm high.

A system of gate valves divides the vacuum chamber into smaller compartments that may be controlled individually so that the component mechanism assemblies may be easily isolated from

the main vacuum chamber assembly. Typically, the optics can be kept cold during system maintenance and device exchange.

The instrument vacuum chamber assembly is composed of a central long pipe in four sections and individual chambers for each of the major mechanism assemblies. The central pipe is partitioned so that the collimator and camera optics are in their own sections, to allow assembly and alignment prior to being joined with the rest of the instrument. The electronics boxes are located along the periphery of the instrument support structure to allow easy access. The instrument support is a large open truss structure with lightweight removable covers. Access platforms, handholds, ladders, and steps will be an integral part of the support structure in order to ease instrument maintenance. The weights of major subassemblies are summarized in **Table 13.5-6**.

Table 13.5-6. NIRMOS weight summary.

	Mass (lbs)	
Main Vacuum Chamber Assembly	17,500	
Section 1 – Slit Mask Housing Assembly	4,300	
Section 2 – Collimator Housing Assembly	4,800	
Section 3 – Main Mechanism Housing Assembly	4,800	
Section 4 – Camera Housing Assembly	3,600	
Slit Mask Cassette Mechanism Housing Assembly 1	1,175	
Slit Mask Cassette Mechanism Housing Assembly 2	1,175	
Filter Cassette Mechanism Housing Assembly	1,050	
Forward Disperser Cassette Mechanism Housing Assembly	2,700	
Pupil Mask Cassette Mechanism Housing Assembly	1,300	
Rear Disperser Cassette Mechanism Housing Assembly	3,350	
Subtotal Vacuum Chamber Assembly		28,250
NIRMOS Electronics Assemblies	3,000	
System Electronics Assembly	500	
Cryogenics Electronics Assembly	900	
Vacuum Electronics Assembly	1100	
Detector Electronics Assembly	500	
Subtotal Electronics Assemblies		3,000
NIRMOS Instrument Structure		17,900
Grand Total		49,150

13.5.4.4   Cryogenic Mechanism Concept

The NIRMOS instrument includes seven mechanisms operating within the cryogenic environment of the vacuum chamber. Most of these mechanisms will be of similar design.   Six of the seven mechanisms are used to exchange components in the optical path (slit masks, filters, dispersers, pupil masks), while the final mechanism provides instrument flexure compensation by moving the detector in three axes.

13.5.4.4.1   Mechanism Overview

Each of the six component exchange mechanisms contains a cassette stack (of slit masks, filters, dispersers, or pupil masks) and a mounting mechanism located on the optical path of NIRMOS. Since each component must pass through a gate valve and a radiation shield, we have elected to include transfer and loader mechanisms. The cassette stack has two motorized axes: a component selection elevator and a component transfer mechanism. The mounting mechanism also has two motorized axes: a component grabber and a component loader mechanism. The radial travel from the cassette stack to the final position in the optical path may be as much as 1.5 m. This strategy reduces the travel requirement for any single motion stage and simplifies the motion profile passing through the gate valve and radiation shield.

The conceptual design uses linear motions for all except the grabber mechanism, which is a rotary mechanism. The focal plane array is actuated in three perpendicular directions for flexure control and focus. A total of 29 axes of motion are required, including a pupil mask rotator for the main spectrograph and for the IFU.

The conceptual design for the slit mask assembly is shown in Figure 13.5-13. This mechanism must accept slit masks from either side of the main vacuum housing. NIRMOS includes two cassette stacks, each with 8 slit masks.
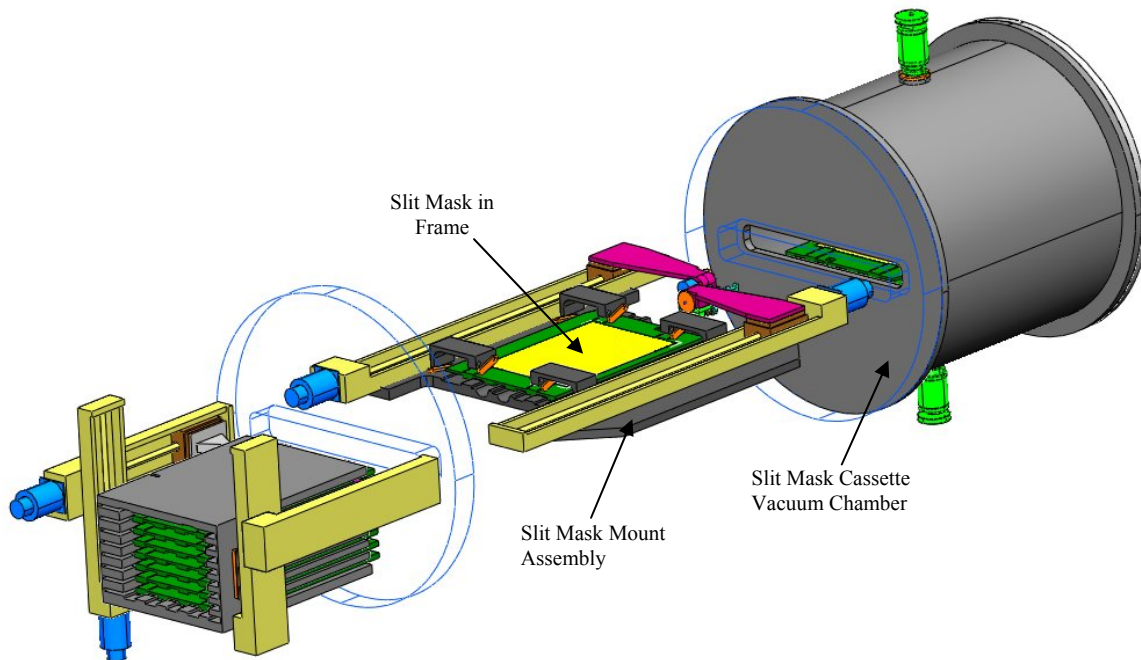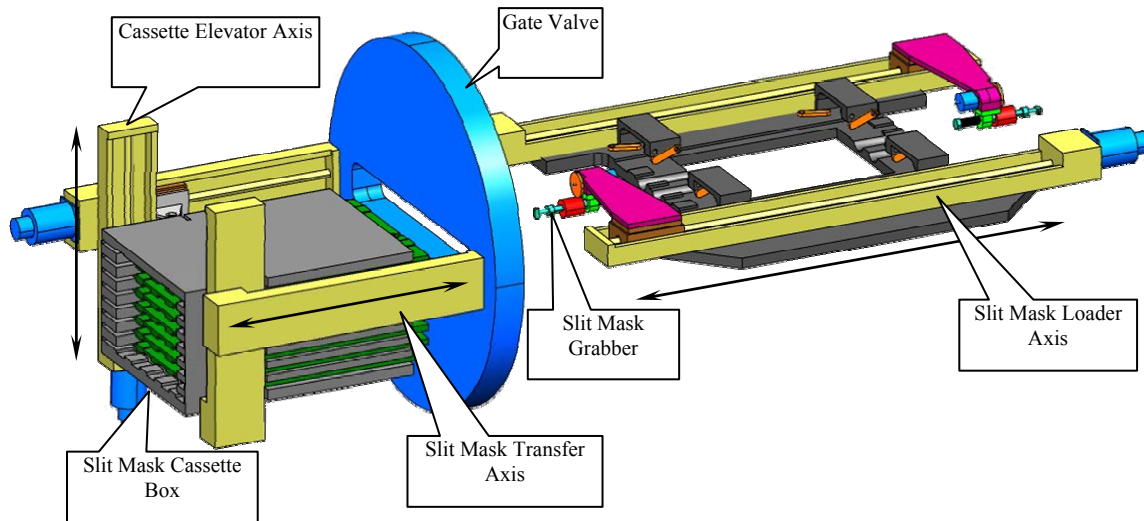

Figure 13.5-13.   Slit mask loaded at focal surface.

13.5.4.4.2   Cryogenic Mechanism Operation Concept

Cassette Elevator Axis

Gate Valve

Slit Mask Grabber

Slit Mask Loader Axis

Slit Mask Cassette Box

Slit Mask Transfer Axis

Figure 13.5-14. The slit mask mechanism includes three linear translation axes and one rotary axis. The stack of eight slit masks are stowed in the cassette box behind the open gate valve. The cassette elevator axis moves the stack of slit masks in the cassette box (not shown) until the desired one is in position to be transferred through the gate valve. The loader axis moves the slit mask grabber into position.
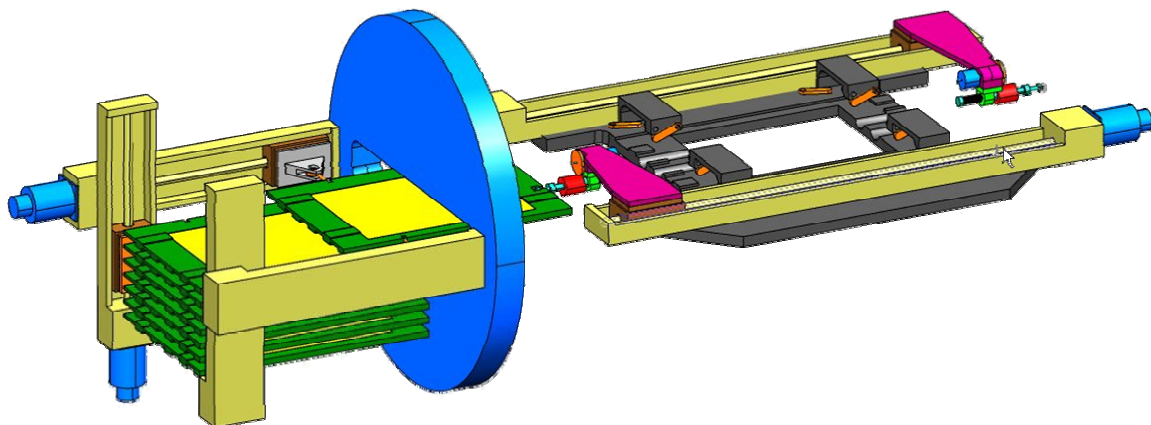

Figure 13.5-15. The slit mask transfer axis moves the desired slit mask through the open gate valve (~375mm). The slit mask frame slides into position onto the grabber.
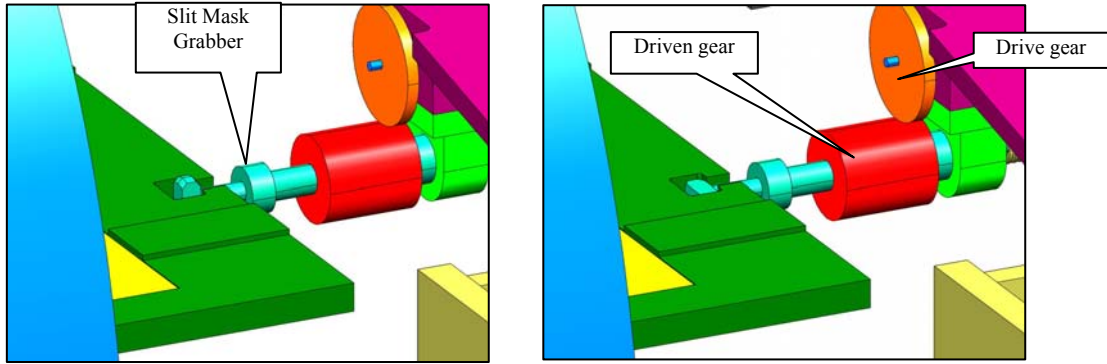
Figure 13.5-16. The slit mask grabber fits into the slot in the slit mask frame. The grabber rotates 90º in order to grab the frame so that it may be pulled into position.
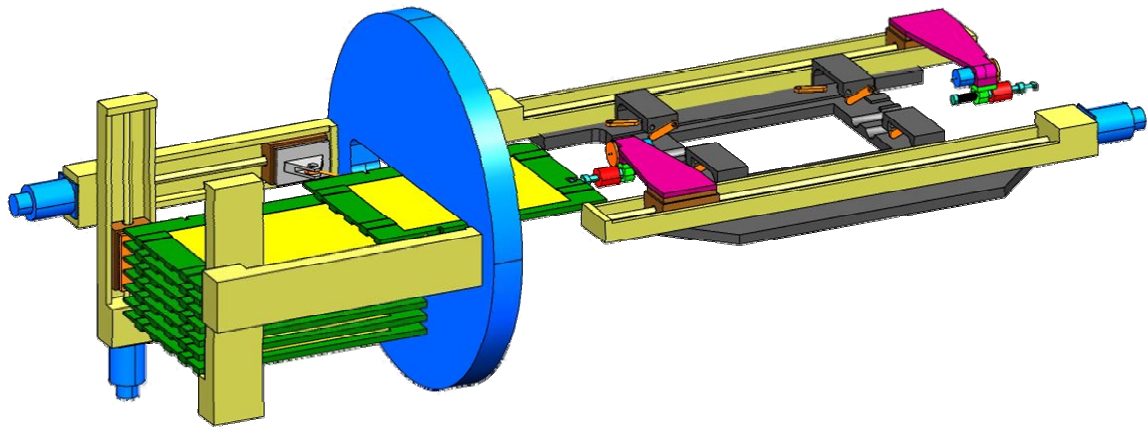
**Figure 13.5-17.** As the slit mask loader axis begins to pull the slit mask into position, the slit mask frame is released from the transfer axis. The frame translation guide for the loader axis is not shown.
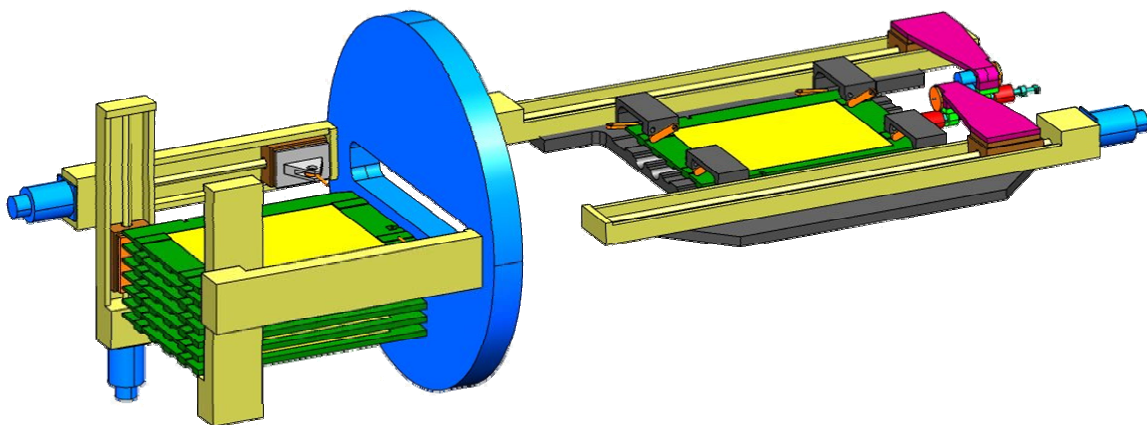
Figure 13.5-18. Finally, the slit mask is pulled into position by the loader axis (950mm). The slit mask is held in position by flex pivot flexures and a compression spring located on the grabber axis (not shown).

Bidirectional loading capability is enabled by a series of asymmetric cutouts on the bottom surface of the frame that are used for reference banking surfaces as shown in Figure 13.5-19.
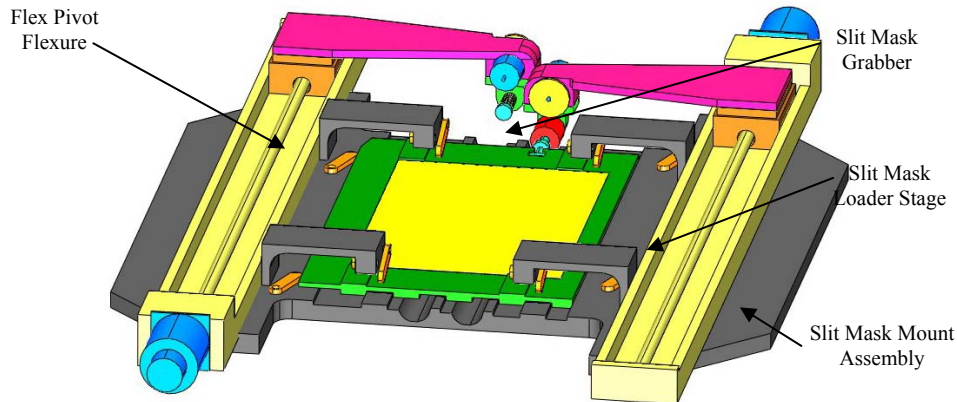

Figure 13.5-19. Slit Mask Reference Base Assembly with Slit Mask

### 13.5.4.4.3 Cryogenic Mechanism Components

All stages, translation components, motors, encoders, etc., will be designed and tested for cryogenic applications. Empire Magnetics makes a line of cryogenic stepper motors which can be delivered with encoders mounted to the rear shaft. Flex pivots are being used wherever limited angle rotary motion is desired (i.e. preload springs). Mission Research Corporation (MRC) has developed a line of cryogenic motion stages for use in their own calibration systems. These stages and motors are available as stand alone products for other applications. We have discussed our requirements with representatives of MRC and they are very interested in pursuing this work. We have also had discussions with THK Corporation regarding the use of their standard products (translation rails and stages) in cryogenic environments. THK products are commonly used in high vacuum applications and they are eager to continue this development into the cryogenic market. We have discussed ways that the THK standard product can be upgraded to suit our needs. This is an area that will require an extensive amount of prototype testing.

13.5.4.5 NIRMOS Cold Tube Assembly

The cold tube assembly is allowed to move both radially and axially as the temperature of the assembly changes. The linear motion is accommodated by fixing one end of the cold tube to the vacuum housing section and mounting the opposite end of the cold tube to the vacuum housing through a set of translation rails. For the longest tube, the collimator assembly cold tube, this motion can be as much as 12 mm over the full temperature range (100° K - 300° K). The radial motion is accommodated by a series of slits machined into insulating rings forming flexures at either end of the cold tube.
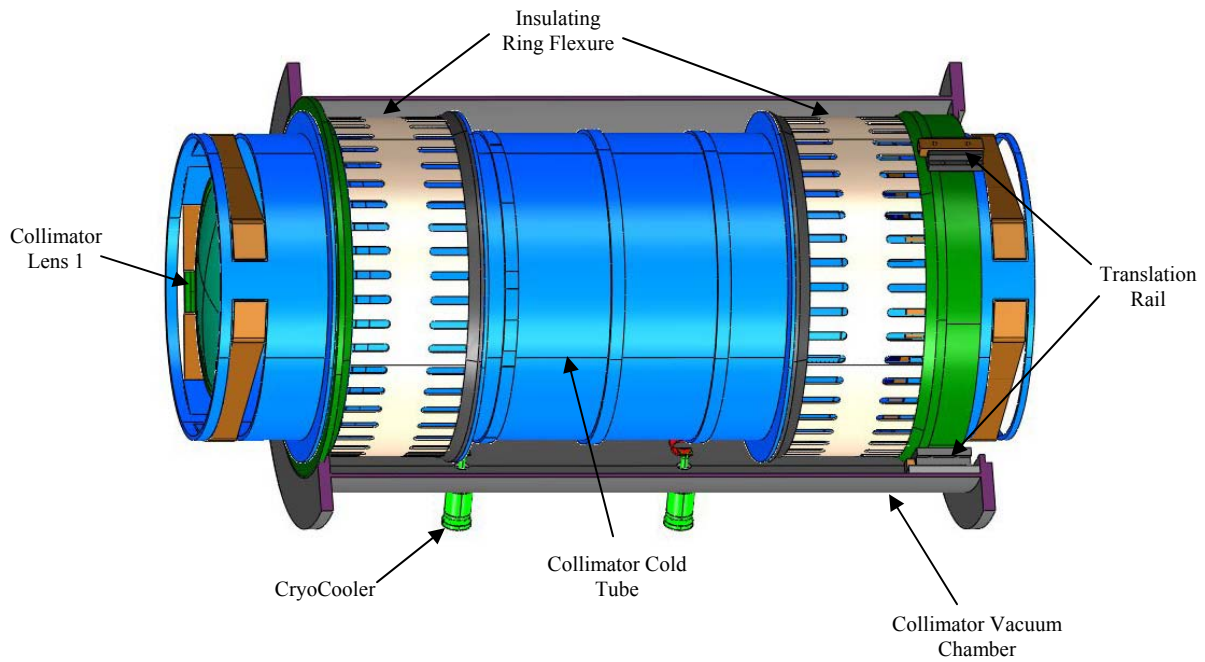
Figure 13.5-20. NIRMOS collimator cold tube assembly. The camera cold tube assembly is similar. The collimator large field lens at the left is distant from the other three elements of the collimator and we intend to investigate the advantages of mounting this lens in a separate assembly.
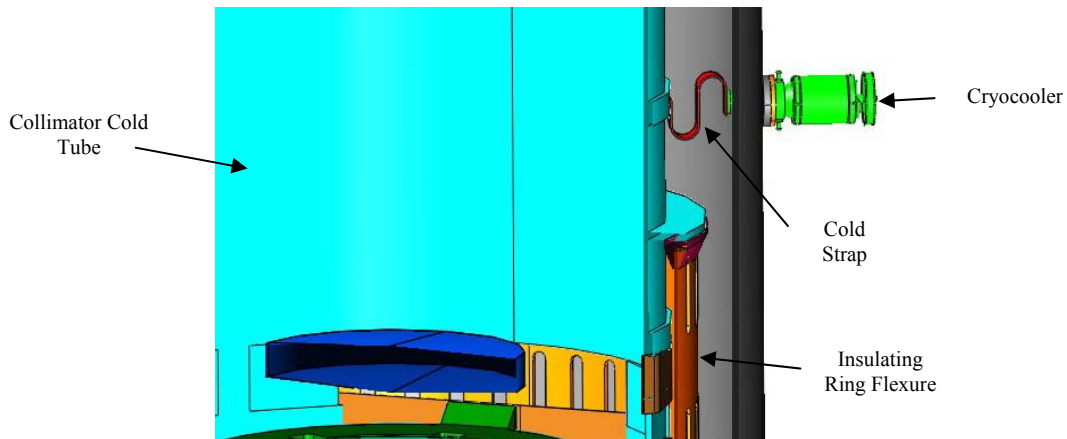
Figure 13.5-21. NIRMOS Cryocooler attachment

13.5.4.6 Instrument Support Structure

Several concepts for the NIRMOS support structure were studied prior to choosing two conceptual designs for further development. These studies produced two promising concepts presented below.
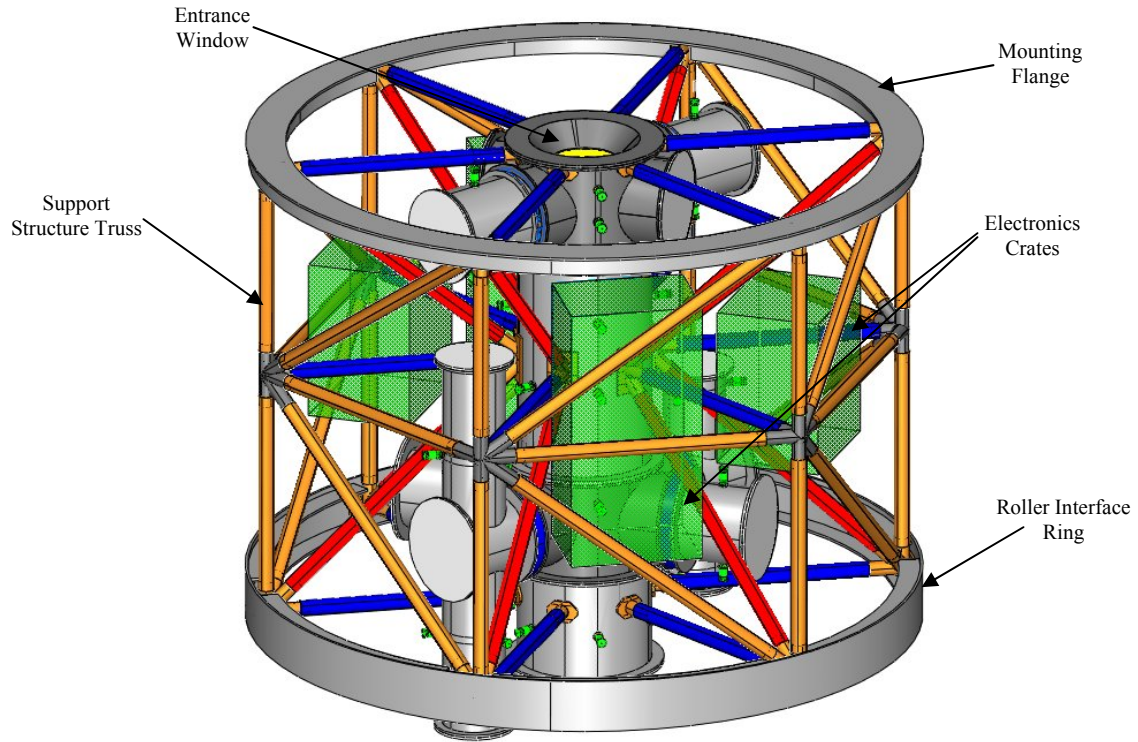
Figure 13.5-22. Instrument Support Structure Conceptual Design – Cylindrical
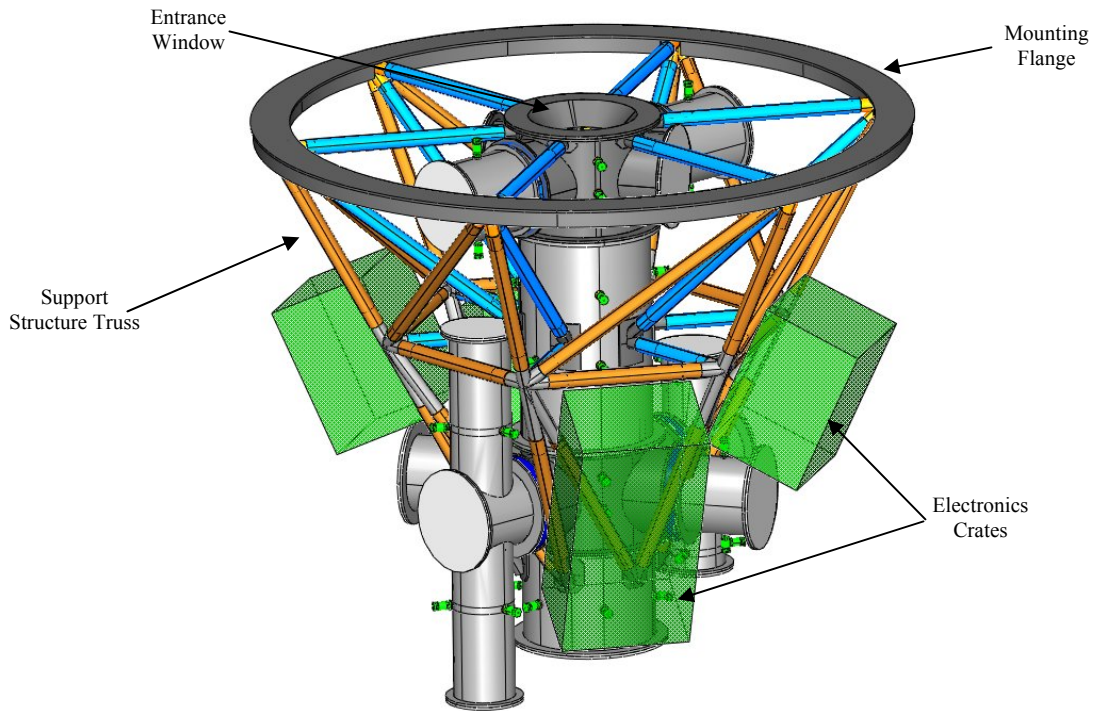
Figure 13.5-23. Instrument Support Structure Conceptual Design - Tapered

Our baseline cylindrical design is shown in Figure 13.5-22. The stiff lower ring included with this structure allows additional support from rollers mounted to the telescope C-rings. This design also allows protected spaces for the electronics enclosures and good attachment points for human access ladders and platforms. An alternate tapered design is shown in Figure 13.5-23. This design is structurally more efficient, but gives up the capability for additional support from the telescope C-rings.

13.5.4.6.1 Structural Design Concepts

Structural elements are made from 6061-T6 aluminum. Both concepts use a 250 inch diameter mounting flange of 1 inch aluminum with two 6.4 inch deep webs. The mounting flange is attached to the telescope with 24 bolts on a 232-inch bolt circle. The two truss concepts differ in detail, but both are built up from tubes with 6 or 8 inch OD and 0.25 inch walls. The bottom ring for the cylindrical design is constructed from 0.875-inch thick aluminum plate. To provide radial stiffness for the telescope rollers, two 8.40-inch deep flanges have been added to the ring. Stiffening gussets have also been added in the areas where the tubes intersect the ring. Typical vacuum chamber wall thickness is 0.25 inch but is locally reinforced where the truss members intersect the tube. The total weight of the instrument is 50,000 lbs with the cylindrical design and 44,500 lbs with the tapered design.

13.5.4.6.2 Structural Analysis and Performance

We have assessed the structural performance of the candidate structures with finite element analysis, focusing on the change in the slit mask and detector displacements relative to the mounting flange for telescope horizon and zenith pointing orientations. These displacements have been extracted from the vacuum chamber assembly displacements at the approximate locations of the slit mask and detector, assuming no local compliance due to mechanisms.

Table 13.5-7. Calculated structural deflections.

Description	Deflection	Lateral X deflection (µm)	Axial Z deflection, (µm)	Rotation about Y, arcsec
Cylindrical structure with additional support	Slit mask relative to mounting flange	103	-243	27
	Detector relative to mounting flange	-34	-301	-6
	Detector relative to slit mask	-137	-58	-33
Cylindrical Structure (no additional support)	Slit mask relative to mounting flange	148	-240	19
	Detector relative to mounting flange	917	-298	-52
	Detector relative to slit mask	769	-58	-71
Tapered structure (no additional support)	Slit mask relative to mounting flange	131	-231	18
	Detector relative to mounting flange	820	-279	-49
	Detector relative to slit mask	689	-48	-68

Table 13.5-7 summarizes the deflection of the cylindrical structure with and without additional support at the lower ring, and of the tapered structure, all with respect to the mounting flange. If

no support in addition to the mounting flange is added, the tapered structure is slightly more efficient, but the potentially easier service access provided by the cylindrical structure may outweigh this advantage.

13.5.4.7   Flexure Control Requirements

The relative flexure of the detector and slit mask is many pixels, and it will be necessary to include passive or active flexure control.   Typically, the most stringent flexure correction requirements are set by fringing in the detector. Fringing of ~10% in HgCdTe detectors has been reported.   Most of this fringing is thought to originate in the sapphire substrate, which is actually above the HgCdTe in the detector package. Multiple reflections occur inside this layer, due to the large mismatch in refractive indices of sapphire and HgCdTe, setting up an interference fringe pattern in the detector array. Since 1998, a project at Rockwell has been underway to replace the sapphire substrate with CdZnTe which has a refractive index closer to HgCdTe, and which could even be removed from the package by etching. These devices are now being tested, and may diminish the fringing to a level where it could be ignored.

With the sapphire substrate, the order of a fringe is dependent on wavelength:
$m(w) = 2 \cdot n \cdot t \cdot \cos(y)/w$, where n is the sapphire index, t is the thickness of sapphire, y is the angle of incidence, and w is the wavelength.   The distance in pixels between fringe peaks then becomes $F(w) = w / [(2 \cdot n \cdot t \cdot \cos(y))/w + 1]/d$, where d is the dispersion in μm pixel^{-1}. Typical fringe peak separations are then between 4 and 10 pixels in the JHK region for NIRMOS. For KSPEC (Hawaii I array), a fringe amplitude of 10% was seen. However, for FLAMINGOS I, no fringing was detected. The difference may be due to the faster FLAMINGOS camera, but further information is needed, and will be on hand when MMIRS and NIFS become operational.

If the amplitude is indeed ~10% in the JHK bands, then analysis using artificial data (conducted by MacGregor), shows that 1% accuracy in fringe removal can be achieved only if the flexure between flat-field and object exposures is less than 0.5 pixel.   If NIRMOS is stable to this level throughout the night, then flat fields taken during the day can be used during the night. A requirement for 0.5 pixel flexure control is not unduly demanding. We currently intend to correct flexure by moving the detector array. Distortion in the optical design will limit the effectiveness of this approach. We will investigate alternatives for flexure control in the next stage of the design development.

13.5.4.8   Lens Mount Concept

13.5.4.8.1   Introduction

We are planning to use a common approach for mounting each of the four collimator and five camera group lenses. This lens mount concept provides proper support of the optics at cryogenic temperatures, controls heat flow to the lenses during thermal cycling to limit thermal stress while minimizing thermal cycling time, and protects the lenses from the loads encountered during shipping, handling, and mounting NIRMOS.

13.5.4.8.2   Design Details

The lens mount design provides two types of support to the optical elements. The kinematic hard mount points provide positional stability for the optical elements while the force loaded supports minimize the local displacements of the optic between the "hard" mount locations. For

the conceptual design, we have chosen to study the thinnest optical element, collimator lens 3. This S-FTM16 lens has a central thickness of 15 mm and a diameter of 425 mm.
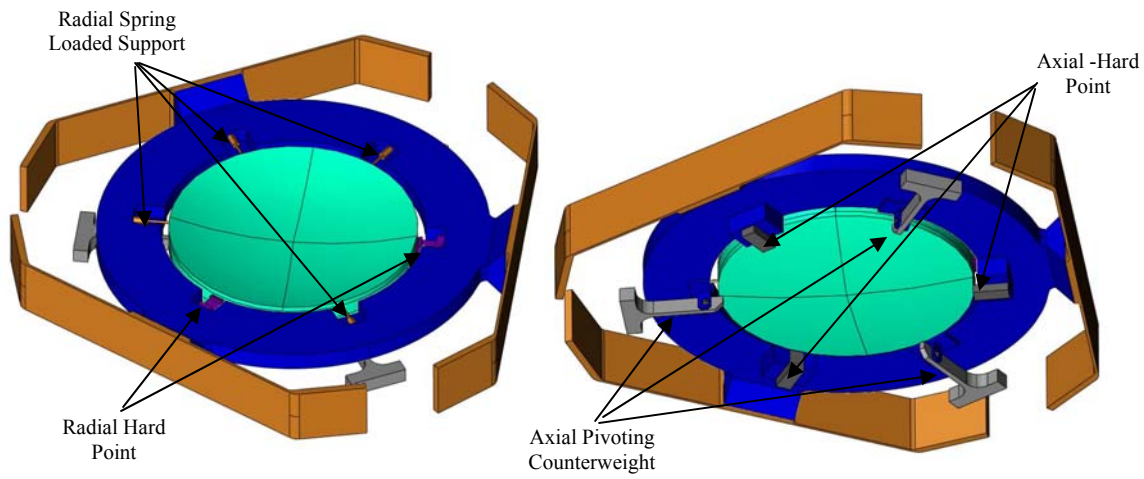
Figure 13.5-24. Lens Mount Geometry, top view on the left and bottom view on the right. The lens cell is mounted to the cold tube assembly with three tangent flexures to accommodate the large thermal swing from ambient to cryogenic temperatures.

Three axial hard points in the form of titanium flexures control the axial position of each lens. The radial position of each lens is controlled with two hard radial mount points and a third spring-loaded radial mount point (also titanium flexures). A finite element analysis of the lens determined that three additional force loaded axial and radial mount points were required to reduce the local lens deflections. For collimator lens 3, the axial supports contact the lens surface with titanium rods providing a maximum force (3.9 lbs) equal to $1/6^{th}$ of the mass of the lens (23.5 lbs). The axial force supports are provided by pivoting counterweights so that the lens support tracks gravity (see **Figure 13.5-24**). The use of a flex pivot mitigates the effects of friction and other additional load vectors over different gravity orientations. The radial force supports are coil springs providing 23.5 pounds of force at each of 4 locations. In practice, this radial preload must be increased to provide a margin for handling, but this optimization has not been carried out yet.
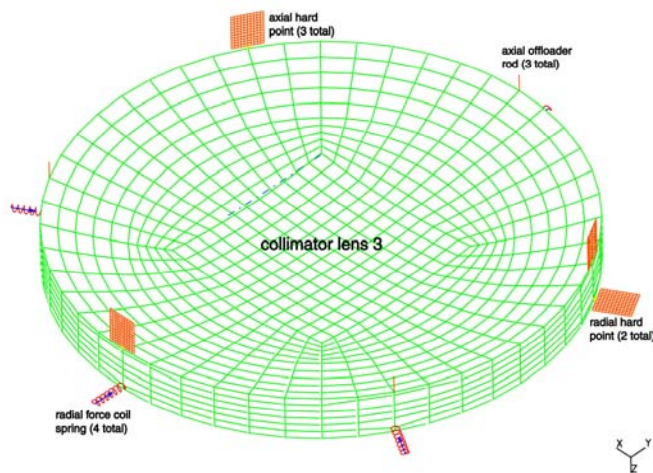
Figure 13.5-25. Finite element model of lens mount concept.

13.5.4.8.3   Structural Analysis and Performance

A finite element model of the lens mount concept finite is shown in Figure 13.5-25.   The calculated lens mount deflections for axial and radial gravity are shown in Figure 13.5-26 and Figure 13.5-27. Optical deformations and stress levels are acceptable. It may be possible to use simpler three point mounts for some of the lenses, and we will investigate this possibility in the next design phase.
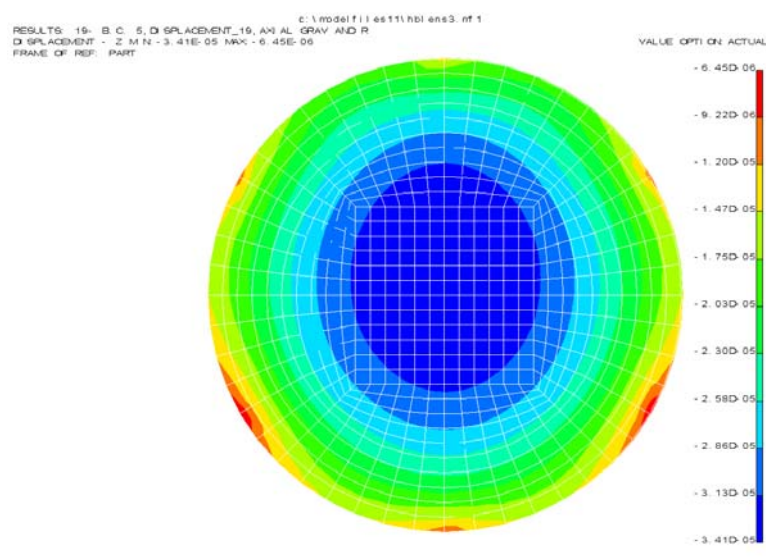
Figure 13.5-26. Deflected Lens 3 on conceptual mount with axial gravity and preload.
Peak to valley deflections are 0.70 µm.
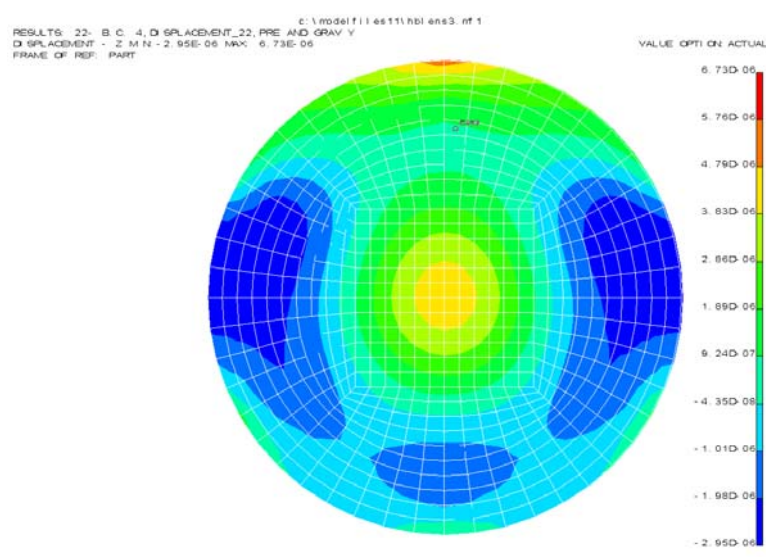
Figure 13.5-27. Deflected Lens 3 on conceptual mount with lateral gravity and preload.
Peak to valley deflections are 0.22 µm.

13.5.4.9 Cool-down and Warm-up Cycle Requirements

To estimate the number of required cryocoolers, we approximate the thermal mass by assuming that the system has a specific heat of aluminum since most of the mass is aluminum and the other major components have similar specific heats. NIRMOS is partitioned into eleven distinct regions that will require cryogenic cooling. Each of these regions has its own cold tube that is cooled by a minimum of two cryocoolers for redundancy.
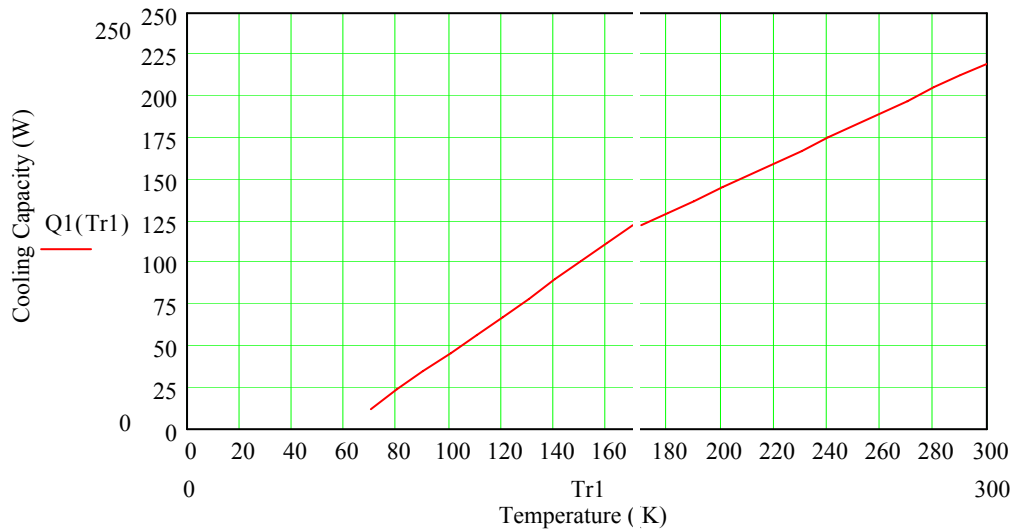
Figure 13.5-28. Cooling capacity for 2S132K cryocooler. Data provided by Qdrive.

The lumped body cooling rate (dT/dt) for an object is determined by the equation:

$$dT/dt = Q(T) / [m \cdot Cp(T)]$$

where m is the mass, Cp(T) is the specific heat, and Q(T) is the cooling capacity.

The "lumped" analysis means that we have ignored any heat flows within the cooled region and assume that heat extracted results in a simple decrease in uniform temperature. In this equation, the Q(T) is net cooling. Parasitic heat gains to the element that would reduce the cooling rate are ignored here. We approximate Cp(T) as that of aluminum since most of the mass to be cooled is aluminum. Q(T) is taken from Figure 13.5-28.

Using the cooling rate equation and the masses of the eleven sections, we have calculated the number of cryocoolers required for each region to keep the cooldown time 2 days or less. These totals are shown in Table 13.5-8. A representative cooling profile is shown in Figure 13.5-29.

Table 13.5-8. Summary of cooled components. Column 1: cooled mass, column 2 desired temperature, column 3: estimated number of required cryocoolers to attain the cool down times in column 4.

Subassembly	Mass (lbs)	Target Temperature	Required Num of Cryocoolers	Cool Down Time (hours)
Slit Mask and Entrance Window	300	100 K	2	24
Slit Mask Cassette Mechanism 1	550	100 K	2	41
Slit Mask Cassette Mechanism 2	550	100 K	2	41
Collimator	1925	100 K	8	36
Main Mechanisms	850	100 K	4	33
Filter Cassette Mechanism	550	100 K	2	41
Forward Disperser Cassette Mechanism	1400	100 K	6	35
Pupil Mask Cassette Mechanism	750	100 K	3	37
Rear Disperser Cassette Mechanism	1900	100 K	6	48
Camera	1300	100 K	4	49
Detector	50	70 K	2	6
Total	10125		41	49

We now investigate whether the optical elements can be safely cooled in the two days permitted by the cryocoolers. The optics must be cooled slowly enough to prevent excessive internal stress due to thermal gradients. Radiative cooling produces the least stress because the lenses cool from their faces and thus do not develop large radial gradients. However, radiative cooling becomes inefficient as the temperature drops due to the T^4 dependence. This is a lumped capacitance calculation with two lumps, one for the radiatively cooled lens, and one for the surrounding structure cooled by the cryocooler. The two are assumed to be perfectly radiatively coupled, thus the calculation is optimistic. Figure 13.5-29 shows that the 100 mm thick CaF_2 camera lenses take six days to radiatively cool down to 100 K from room temperature. This is too slow.
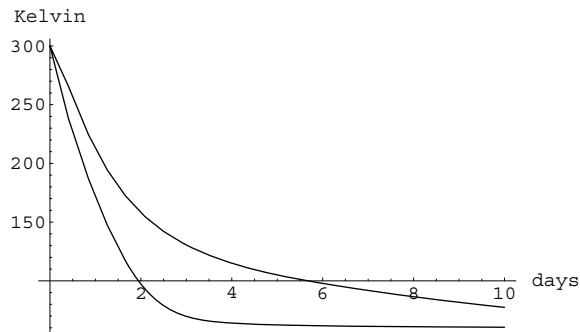
Figure 13.5-29. Radiative cooling for thickest lenses. The upper curve is the lens temperature. The lower curve is the surrounding mount connected to the cryocooler.

13.5-29
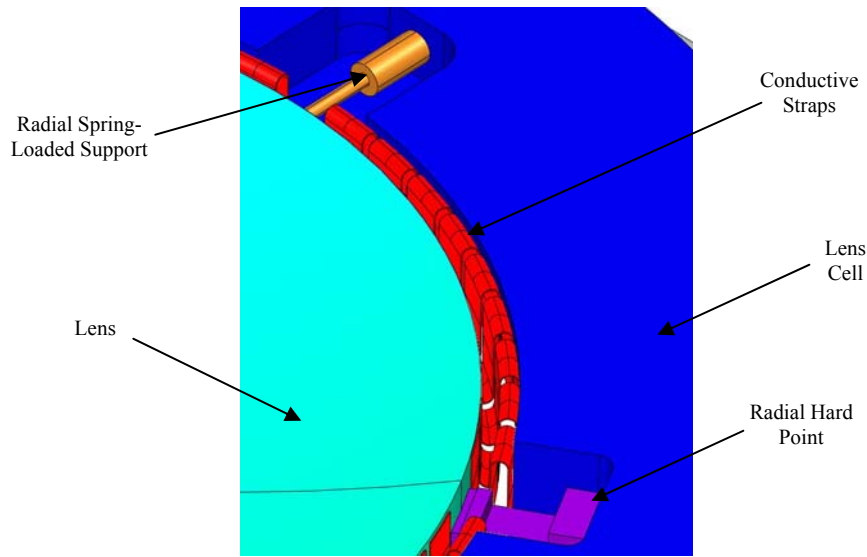
Figure 13.5-30. Conductive heat straps surrounding the circumference of the lenses.

We next consider purely conductive cooling, where we assume that the heat is removed over the full circumference of the lens by conductive straps (**Figure 13.5-30**). A radial temperature gradient will develop in the lens as it is cooled, resulting in a maximum stress at the center of the lens. A preliminary FE analysis of the 9 cold lenses shows that the two S-FTM16 lenses develop the largest stress because they are thin and have low thermal conductivity. If we cool the lenses linearly over 48 hours the stress reaches ~1200 PSI. The CaF_2 and BaF_2 elements all have stresses of 500 PSI or lower. The conductive approach therefore appears promising, although more analysis is required. We will need to construct integrated thermal models considering the non-linear cooling rate from the cryocooler and both radiative and conductive cooling processes. The conductive paths to the cold tubes and estimated parasitic heat loads will also need to be modeled.

13.5.4.9.1   Cryocoolers

We have identified two candidate cryocoolers: the Cryotel-GT, manufactured by Sun Power Inc., providing 15 watts of cooling capacity at 77 K, and the model 2S132K, manufactured by Qdrive, providing 20 watts of cooling capacity at 77K. Both units provide sufficient cooling capacity for NIRMOS and both do not require separate compressors with cooling lines. Both are self-contained units that may be water-cooled at the body of the cryocooler. They exhibit little vibration; have low maintenance requirements, and a 5-10 year estimated operational life. They are programmable for cooling rate and target cooling temperature (to ~ 40º K) and may be cycled on/off continuously.

13.5.4.9.2   Waste Heat Removal

The major source of waste heat generated by the NIRMOS instrument will be from the cryocoolers. As shown in Section 13.5.4.8, NIRMOS may require as many as 41 cryocoolers to achieve cryogenic temperature in the desired cool down time of 48 hours. Each individual cryocooler requires 200-250 watts of power be supplied to operate each Stirling Cycle device in order to achieve the maximum cooling rate. Maximum heat generation will occur during the

initial instrument cool down from room temperature. We must allow for the removal of up to 10 kW of waste heat. The waste heat produced during normal NIRMOS operation is much less than 10 kW. The waste heat from the cryocoolers will be extracted with a recirculating liquid coolant supply. Power dissipated by the NIRMOS electronics assemblies must also be extracted from the instrument enclosure with liquid coolant. The electronics subsystems will generate ~4 kW of waste heat.

13.5.4.10 Vacuum System

The vacuum system for NIRMOS is composed of two 280 liter s^{-1} turbo pumps and two 8.3 liter s^{-1} roughing pumps. The pump pairs can be used in tandem when evacuating the instrument from atmospheric pressure, or individually to pump out the slit mask section when slit masks are exchanged or individual mechanism sections when the mechanisms are serviced. The total volume to be evacuated is ~2500 liters. Taking into account the flow rate restrictions caused by the length and diameter of the vacuum pipes running from the pump station to the vacuum chambers, we estimate that it will take ~3 hours to pump NIRMOS from atmospheric pressure down to 1×10^{-5} torr.

Each turbo pump/roughing pump pair with controller weighs ~100 lbs. The vacuum pumps will be housed in one of the electronics modules and connected to the individual vacuum chambers with 125 mm diameter plumbing. A vacuum manifold will control the flow from each of the vacuum chambers. Custom motor-driven gate valves, similar to the units fabricated for the MMT/Magellan MMIRS instrument, divide the main vacuum chamber from the mechanism modules. Electrical interlocks monitor temperature and pressure gauges in each of the vacuum chambers to prevent inappropriate valve operation. Improper venting of cold optics and detectors could cause very serious damage. A dry nitrogen backfill system will be provided.

13.5.5 Detector Array

13.5.5.1 Available and Projected NIR Imagers

The best available near IR imagers utilize a HgCdTe photodiode array bump-bonded to a silicon multiplexer readout structure, providing peak quantum efficiencies in excess of 75% out to a 2.5 μm cutoff. This situation is unlikely to change in the next 5-10 years, as monolithic structures combining both photodiodes and readout multiplexers of the same material or using non-silicon multiplexers are not being actively pursued. The currently available large format arrays are the Rockwell Hawaii2-RG (2K x 2K x 18μm) and the Raytheon Virgo (2K x 2K x 20μm). Both Rockwell and Raytheon are currently planning 4K x 4K arrays with 15 or 20μm pixels. However, for this proposal we base our design on currently available 2K x 2K package. JWST is likely to use the Rockwell 2K X 2K devices and we expect NASA funding to develop improved versions of the Hawaii-2RG to benefit NIRMOS.

13.5.5.2 Dark Current

The expected dark-sky background at R=10000 with a 0.5″ wide slit will be approximately 0.3e-/s/pix. G. Finger at ESO has tested a Hawaii-2RG device with a dark current of 0.01e-/s for T≤80 K, significantly less than our expected sky background. Thus, at no time do we expect to be dark current limited. The ESO measurements indicate that the mean dark current does not drop significantly as the temperature goes below 80 K. However the cosmetic quality does

increase significantly as the temperature goes down to 60 K. ESO saw no drop in QE as the temperature dropped, so an operating temperature as low as 60 K might be desirable.

13.5.5.3   Readout Noise

ESO's measurement of the Hawaii-2RG shows a read noise of 13e- with 1 pair of reads, dropping to 2.2e- with 256 pairs of reads at 0.825 s/read. We can expect that with this array, NIRMOS would be read-noise limited for exposure times less than 60 s. The brightest night sky lines have a flux of 400-500 photons/s/m^2/arcsec^2 (Maihara et al. 1993 PASP, 105, 940), which correspond to a rate of 200e-/pix/s in NIRMOS. Thus we can integrate for several minutes to get above the read noise without saturating even the brightest lines. The limiting factor then becomes the stability of the night sky lines.

13.5.5.4   Imager Array Readout Electronics

The JWST project is investing heavily at Rockwell to develop a sophisticated readout ASIC (application-specific integrated circuit) for their present and projected near IR imagers. Versions are now or shortly will become available that plug into the backside of the imager and provide not only all the drive and bias signals to read out the multiplexer but also a full 16-bit A/D conversion of all 36 channels of video output as well. Thus, all the functions that heretofore have been provided by complex external hardware will soon become part of the imager itself, and the problem reduces to providing a relatively simple high-speed data acquisition system to feed the digitized video information into host computer memory. Not only is such a system easier to design than the multi-channel analog video processors that are currently used, one could expect that system noise performance would be improved due to the tight coupling of the imager to its nearby integrated cold signal processor. The initial ASIC tests performed by Rockwell achieved 5e- read noise, not as good as that achieved by ESO with discrete electronics. However, the ASIC testing is in its infancy, and we will monitor progress so as to determine the best way to achieve low noise performance.

13.5.6   Electrical Design

13.5.6.1   Introduction

The NIRMOS electronics are partitioned into four functional blocks: detector electronics, system electronics, vacuum systems, and cryogenic system. Two of these systems will occupy a volume of ~1.25 x 1.5 x 0.9 m, and two will occupy a volume of ~1.25 x 2.5 x 0.9 m. Waste heat from each system will be extracted with liquid coolant.

13.5.6.2   System Electronics Assembly

The System Electronics Assembly (SEA) provides all of the motion and actuator control for NIRMOS. Three Delta Tau PMAC UMACS in compact PCI hardware format are used to provide the control function for up to 40 axes of motion control. Axes that require continuous position feedback could use cryogenic resolvers, LVDT's, thermally decoupled magnetic encoders, or light shielded optical encoders. The PMAC racks will also provide discrete input/outputs for the control of the gate valves separating the various vacuum chambers of the instrument. A dedicated rack subassembly will provide hardware interlocks to each gate valve actuator based on temperature and differential pressure in order to provide failsafe operation. The

vacuum and cryogenic assemblies will provide alarm signals to the SEA PMAC and Interlock subsystems to support this function. This rack will also provide the safe-to-operate function on all motion axes based on temperature, interlock switch, cross-axis lockout, and emergency stop signals from the instrument.

The SEA provides the switched AC power to the vacuum and cryogenic systems. These outputs are created using Pulizzi 8-channel Intelligent Power Controllers, controlled by an ethernet interface. Buffered PMAC inputs and outputs will be provided to the cryogenic and vacuum assemblies for discrete control, status, and alarm functions. Switched power outputs will be provided to the vacuum assembly for the actuation of solenoid valves, as required. The SEA will also provide ethernet media conversion and switch functions to provide communications and control to the other assemblies.

The main instrument interface to the facility through the SEA will be AC power (208VAC, 3PH) plus one or more ethernet duplex optical fibers. The AC power will be surge protected, filtered, and current limited in the power section of the SEA. An emergency stop loop will be provided from the NIRMOS support rack to allow emergency stops function at the support rack, operator station, and other remote locations.

13.5.6.3   Cryogenic System Electronics Assembly

The ~40 cryocoolers will be controlled by a SunPower DSP based controller. The cryogenic system electronics will also control heater power to the instrument chambers to assist in the controlled warm-up of the instrument. Warm up heater power will be controlled by Omega ethernet interfaced temperature controllers via solid state relays as for MMIRS. Detector array temperature will be controlled by a Lakeshore Model 321 temperature controller as for MMIRS. Switched AC power and input/outputs for control, status and alarm functions will be provided to this assembly by the SEA. Heat will be extracted by liquid cooling. Assembly internal temperature will be controlled by a local temperature monitor/controller.

13.5.6.4   Vacuum System Electronics Assembly

The vacuum system assembly includes two turbo pump/roughing pump pairs, and their control electronics. Eight electric valves and eight Pfeiffer vacuum gauges and controllers are provided to control and monitor the vacuum in each of the seven vacuum chamber lines plus one spare. Control electronics will be used to implement a hardware interlock on the gate valve motion control to prevent catastrophic failures. This system is based on the MMIRS design. Switched AC power will be provided to the vacuum system assembly from the SEA.

13.5.6.5   Detector Electronics Assembly

The detector electronics assembly provides power and control signals to the detector array. The array signal is read out by the detector electronics and transmitted to a data handling and control computer by a fiber optic link. The detector electronics assembly receives switched AC and DC power from the system electronics assembly.

13.5.7   Software Design

13.5.7.1   Software Architecture

We plan to use a client-server software architecture. Server computers onboard the instrument provide instrument control, data acquisition, monitoring, and logging. The instrument with its server computers operates autonomously from the user interface computers in the telescope control room or instrument lab. Standard workstation computers in the control room provide user interface visualization and interaction for the instrument.   The user interface software for the instrument will be provided over the network via the windowing system (**X Windows** or equivalent) or will be installed on the user workstation with a single file installation. The control room and instrument are connected via a gigabit fiber ethernet network.

13.5.7.2   Software Development and Standards

The software development environment will use common standards for clarity. Server programs which must access hardware or do computationally intensive operations are written in **C**. Direct access to device driver level routines in **C** is, however, becoming less important as more data acquisition and control devices are integrating ethernet and **TCP/IP** as their communications interface. User interface clients and simple servers are written in **Tcl** and use the **Tk** toolkit to provide a graphical display. Excepting device specific routines, programs limit their library calls to those available in the standard **C** library. In this way all programs are able to run under the several **UNIX** (and **UNIX**-like) operating systems available and under Microsoft Windows if required.

The software is revision controlled using the CVS revision control system. A tagging command allows the release revision of each program to be easily recorded and referenced. The revision history of each program is available in CVS's "version" file. The software build environment uses project standardized Makefiles with standard build targets. This system allows client and server programs to be reliably uploaded, built and installed on a computer.   The build environment records the installed programs and configuration file and provides a means of checking for correct installation.

The software relies on a few simple but powerful ideas. Clients and servers communicate using an ASCII over sockets protocol. The protocol is documented and a library of routines in **C** and **Tcl** provides high level publish/subscribe semantics. Servers are simple enough that they pass the "telnet test". It is possible to telnet directly to the server port and diagnose its state without the aid of a sophisticated interface client. The client/server model forces the software implementation to be decoupled. The command set and state published by each server forces developers to think through how each part of the hardware system will be controlled and monitored.   It also allows the rapid and creative recombination of hardware functions via additional scripts and client programs during test and integration.

Images are read and written in **FITS** format via the high level **FUNTools** library. All image display is accomplished via the **ds9** image display program. The special image display functions needed for guiding are provided by extending the **ds9** display program with custom **Tcl**

procedures. This has proven to be very successful as all basic image display (scaling, zoom, pan) is provided by **ds9** and the software only needs to provide custom buttons and markers.

Very simple configuration files are kept as **Tcl** scripts. This procedure eliminates the need for configuration file parsing as the files are included in the **Tcl** programs to access the configuration values. Configuration tables and other "database" like files are kept in **rdb** table format and accessed and manipulated with the **Starbase** ASCII data tables programs and routines.

13.5.7.3 Computer Hardware

CPU, RAM and magnetic disk requirements for the NIRMOS instrument are easily met by standard consumer parts available today. The wide-field MMT instruments are currently operated by dual Opteron rack mounted servers located in the telescope yoke room. These computers easily provide the necessary data acquisition, reduction and storage for the MMT Hectospec and Hectochelle spectrographs, as well as the Megacam and SWIRC imagers. Rack style computers mounted within NIRMOS will provide all instrument control and monitoring.

Semiconductor technology continues to be improved at a rapid pace. Magnetic disk storage and DRAM should see significant increases in performance and miniaturization in the coming years. CPU clock speed has recently peaked as power per unit area has reached the limit of heat that can easily be dissipated via simple forced air cooling. Major CPU vendors (Intel and AMD) have begun a more rational focus on CPU computational power per watt and this new focus should directly benefit more power conscious embedded applications like NIRMOS.

13.5.8   Guiders and Wavefront Sensors

NIRMOS will use external active optics and adaptive optics wavefront sensors. Two active optics wavefront sensors will be mounted on stages in the instrument platform wavefront assembly below the top plate of the instrument platform. Wavefront sensors for ground layer adaptive optics will be mounted on the instrument platform. Two on-board NIRMOS guiders will view through holes milled on opposite edges of the slit masks in spectroscopic mode, and will be placed just outside of the field of view in imaging mode. The guiders will be used for slit mask alignment using the holes machined in the slit mask for reference.

13.5.9 Appendix A: Optical Prescription

File : col081005h_cam080905b.ZMX

```
SURFACE DATA SUMMARY:

Surf      Type        Radius     Thickness            Glass       Diameter           Conic
 OBJ STANDARD     Infinity     Infinity                                    0                0
 STO STANDARD       -36000    -20291.26              MIRROR        25306.4       -0.9982088
   2 STANDARD     4208.627     20291.26              MIRROR       3253.439       -0.7111632
   3 STANDARD     Infinity         5200                            1133.102                0
   4 STANDARD     Infinity           75                CAF2             616                0
   5 STANDARD     Infinity      247.393                          610.3263                0
   6 STANDARD     2233.803          200                          584.2224                0
   7 STANDARD     1360.854           85         CAF2_76K_ABS          618                0
   8 STANDARD    -6743.972     1886.192                               618                0
   9 EVENASPH     2735.931           80         CAF2_76K_ABS          452                0
  10 STANDARD    -2112.081     151.8637                               452                0
  11 STANDARD    -659.4248           15    SFTM16L10_76K_ABS          414                0
  12 STANDARD    -1289.135     219.4346                               414                0
  13 STANDARD    -1597.292           80         CAF2_76K_ABS          404                0
  14 EVENASPH    -614.2052          350                               404                0
  15 STANDARD     Infinity          350                          310.0028                0
  16 EVENASPH     433.5846     99.97783         CAF2_76K_ABS          436                0
  17 STANDARD    -7736.517     91.73471                               436                0
  18 STANDARD    -1330.989           15    SFTM16L10_76K_ABS          418                0
  19 STANDARD     601.2043     9.999873                               418                0
  20 EVENASPH     378.0806     100.0008         CAF2_76K_ABS          432                0
  21 STANDARD    -978.1892     325.5812                               432                0
  22 STANDARD     309.3458           70         BAF2_76K_ABS          326                0
  23 STANDARD     1978.708      139.777                               326                0
  24 EVENASPH    -242.1732           20         CAF2_76K_ABS          228                0
  25 STANDARD     623.0896     29.38299                               228                0
 IMA STANDARD     Infinity                                            214                0

Surface   9    : EVENASPH
 Coeff on r  2 :             0
 Coeff on r  4 :  -4.9219842e-011
 Coeff on r  6 :  -2.0286274e-016
 Coeff on r  8 :   1.2619991e-021

Surface  14    : EVENASPH
 Coeff on r  2 :             0
 Coeff on r  4 :   1.7288017e-010
 Coeff on r  6 :    3.667801e-016
 Coeff on r  8 :   2.3464789e-021

Surface  16    : EVENASPH
 Coeff on r  2 :             0
 Coeff on r  4 :  -3.5805109e-010
 Coeff on r  6 :  -3.4277884e-015
 Coeff on r  8 :  -9.1528896e-021

Surface  20    : EVENASPH
 Coeff on r  2 :             0
 Coeff on r  4 :  -2.8549746e-009
 Coeff on r  6 :  -3.1688585e-015
 Coeff on r  8 :  -8.9284915e-020

Surface  24    : EVENASPH
 Coeff on r  2 :             0
 Coeff on r  4 :  -1.5075139e-008
 Coeff on r  6 :    2.485808e-012
 Coeff on r  8 :  -5.6303337e-017
```

13.5.10 Appendix B: Imaging Performance Summary

13.5.10.1 Imaging Mode Encircled Energy

We first describe the optical performance over the 7′ by 7′ imaging field of view that uses a 6144 by 6144 square format.
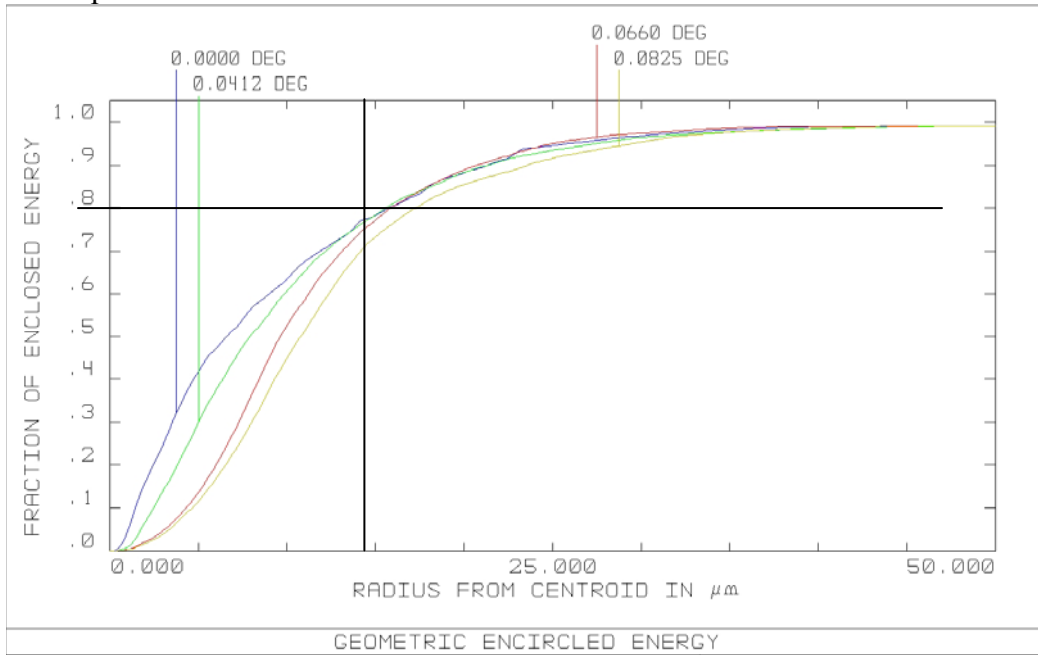

Figure 13.5-31. Z-band encircled energy plot. 80% of the power is within a diameter of 34 microns or 0.13″.
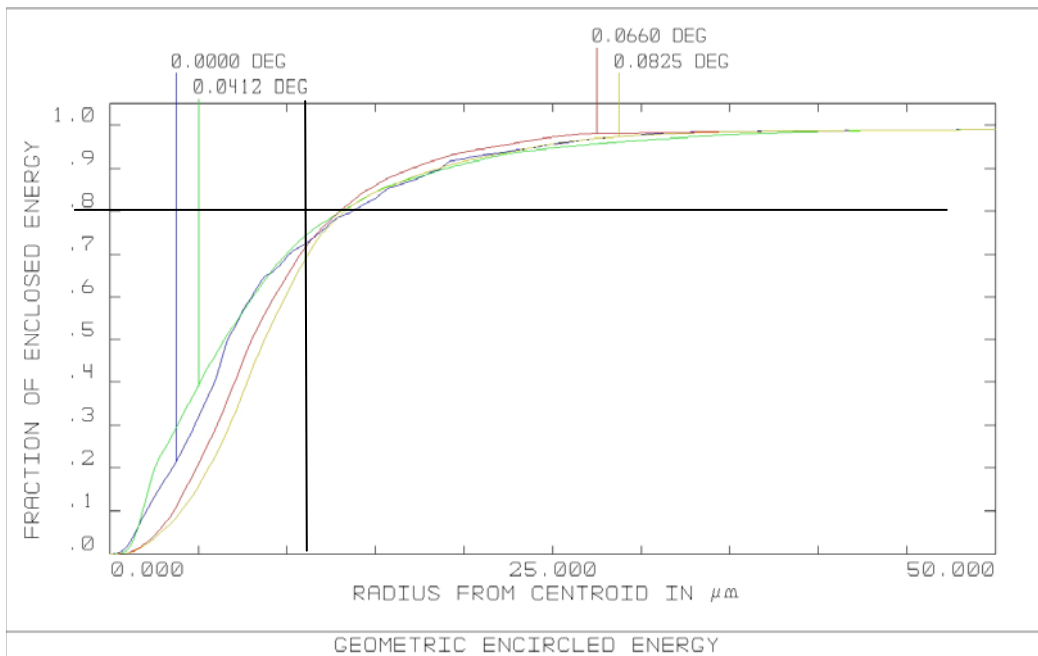

Figure 13.5-32. J band encircled energy plot. 80% of the power is within a diameter of 28 microns or 0.10″.
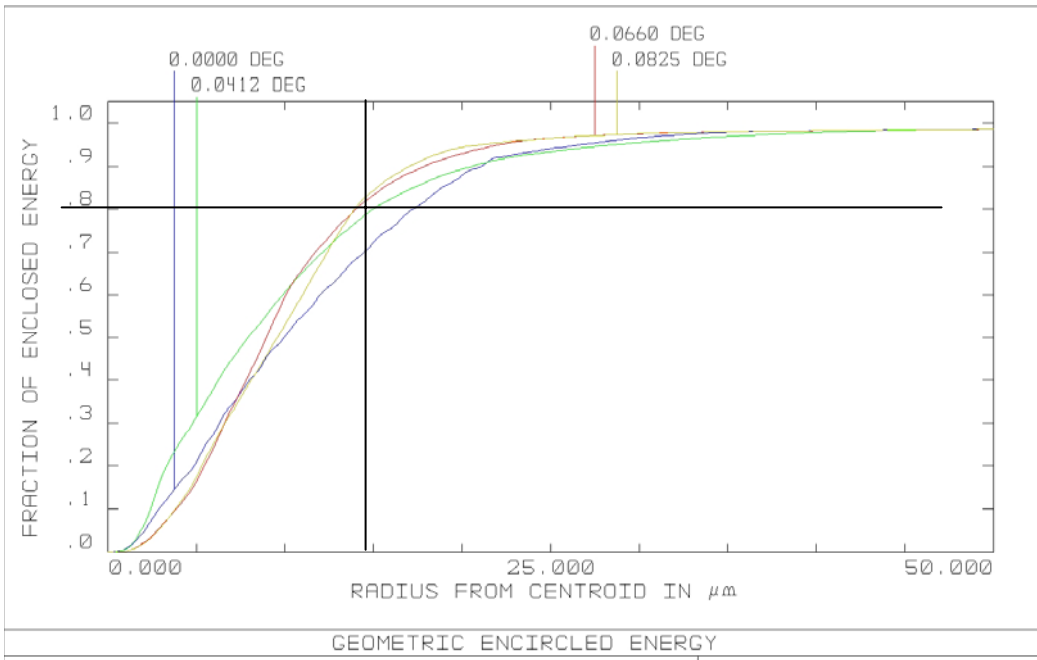
Figure 13.5-33. H band encircled energy plot. 80% of the power is within a diameter of 35 microns or 0.13″.
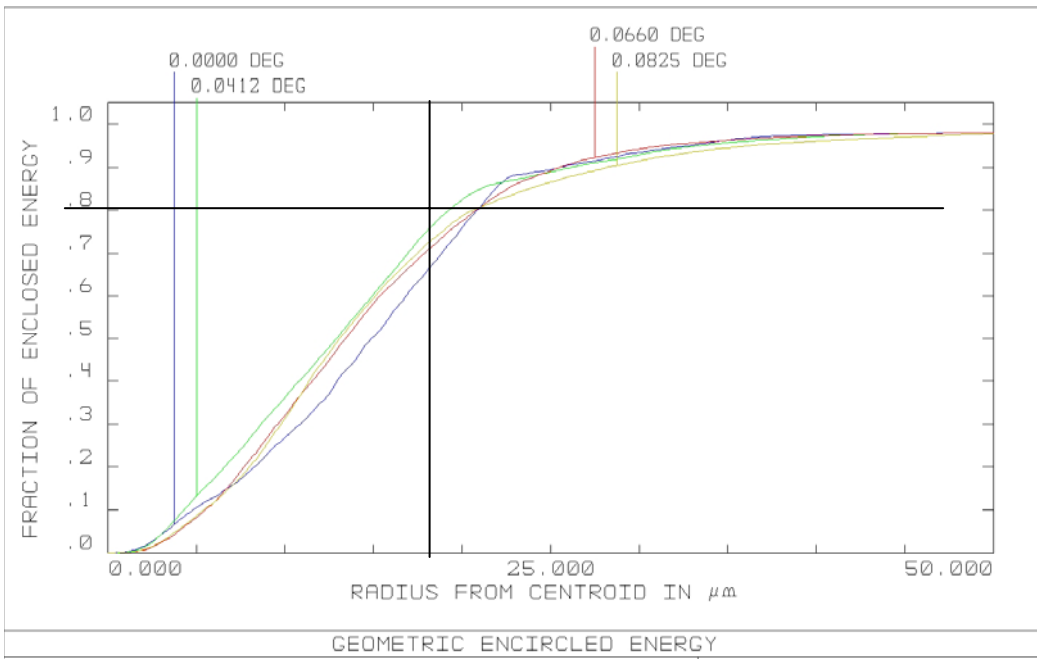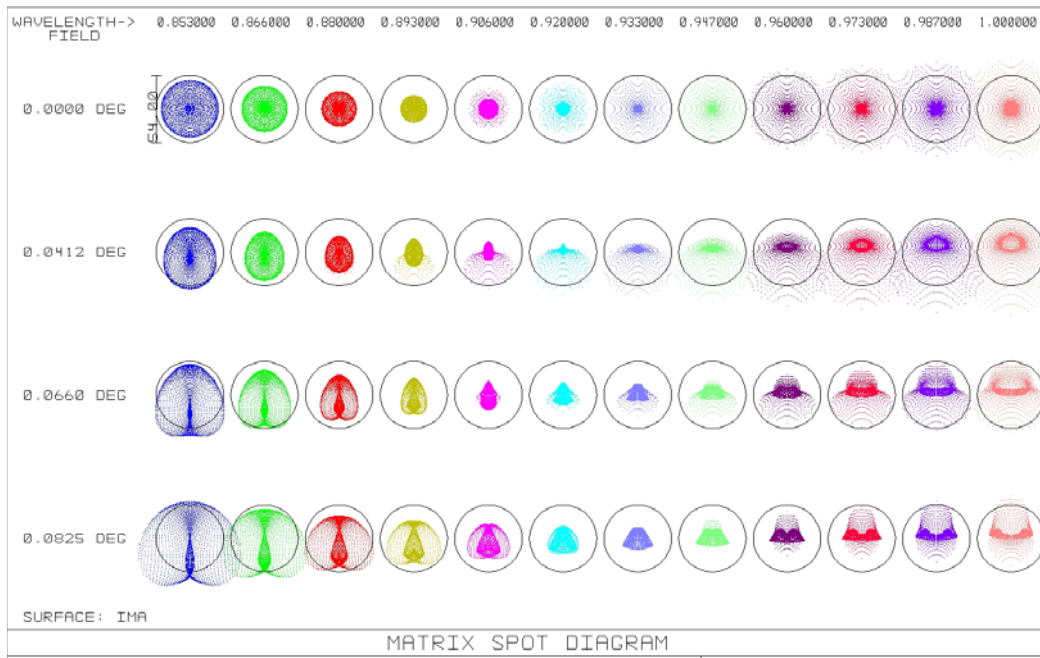

Figure 13.5-34. K band encircled energy plot. 80% of the power is within a diameter of 42 microns or 0.16″.

13.5.10.2   Imaging Mode Spot Diagrams

Figure 13.5-35. Z-band spot diagrams in imaging mode for four field angles moving out along the imaging field diagonal. The top line shows on-axis spots, the second line spots 2.48′ off-axis, the third line 3.96′ off-axis, and the bottom line 4.95′ off-axis. The spots are separated horizontally to show the effects of lateral color and to allow a more careful inspection of the images.
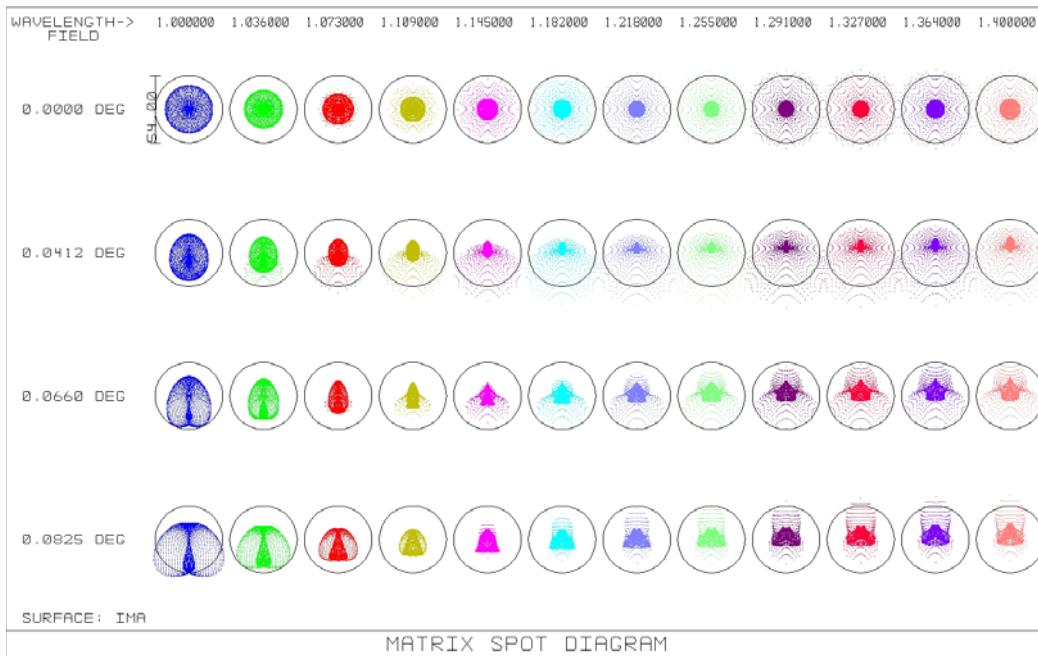
Figure 13.5-36. As for **Figure 13.5-35** except in the J band.
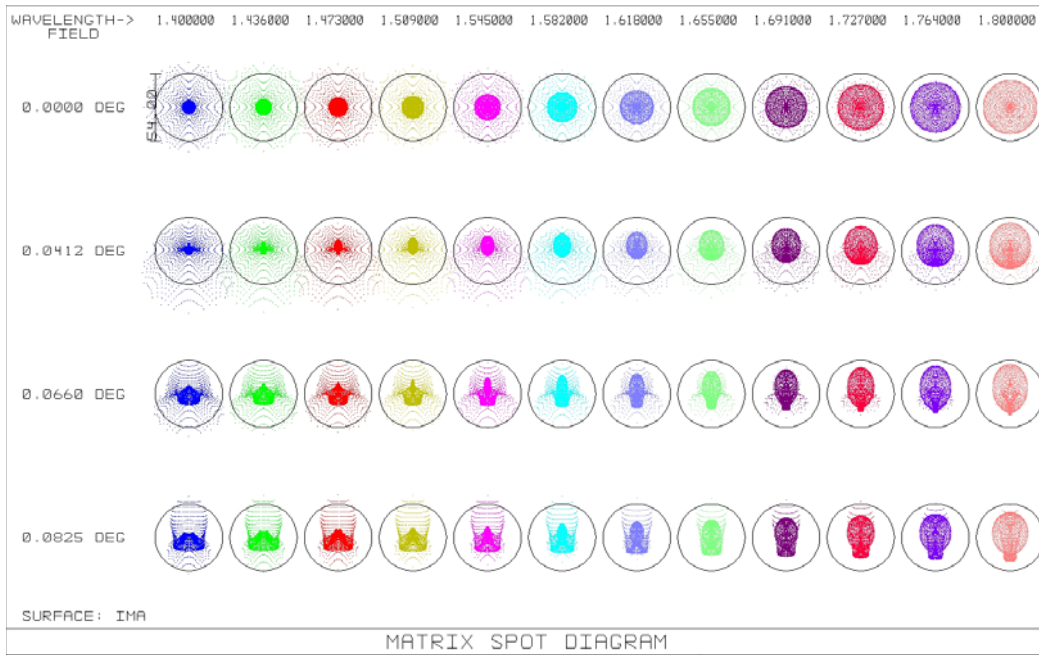
Figure 13.5-37. As for
Figure 13.5-35 except in the H band.
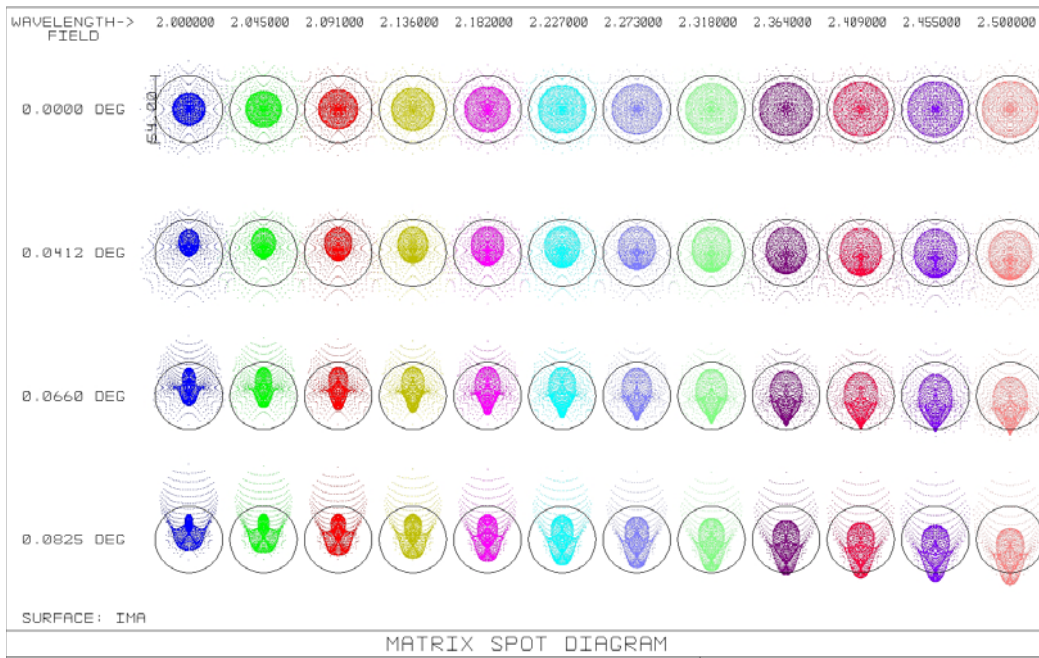
Figure 13.5-38. As for **Figure 13.5-35** except in the K band.

13.5.10.3   Spectroscopic Mode Spot Diagrams
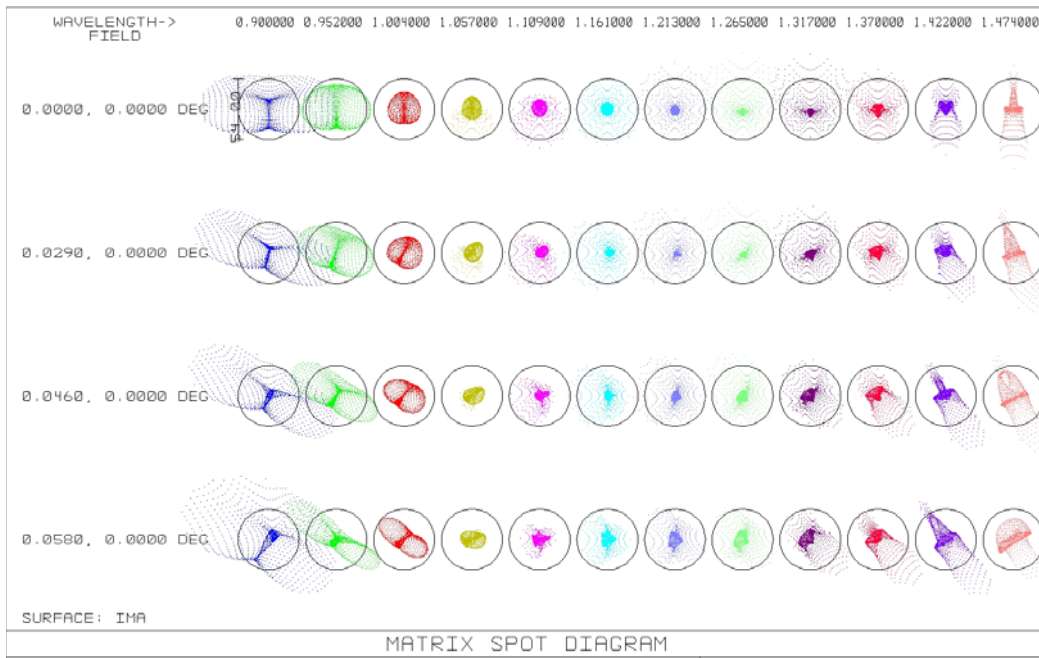
Figure 13.5-39. Images using full 10240 pixel spectral format of the detector across the page.   From top to bottom: spots for central spectrum, 1.75′ off-axis along the slit, 2.8′ off-axis along the slit, and 3.5′ off-axis along the slit. The circle shown is 0.2″ in diameter. The images are poorly focused bluewards of 0.95 μm.
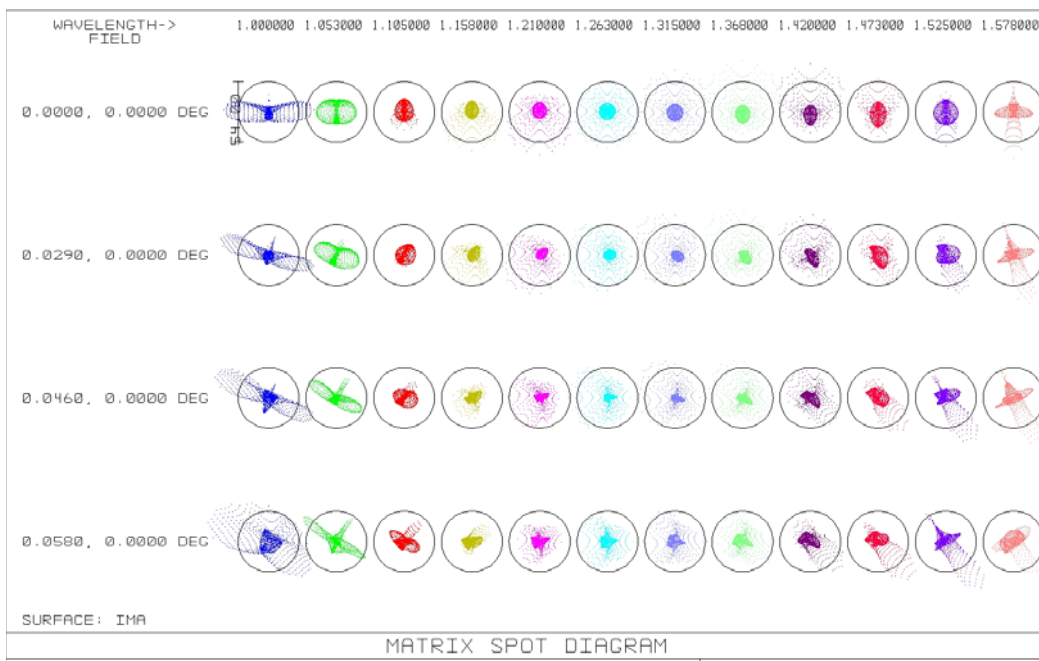
Figure 13.5-40. Same as **Figure 13.5-39** except shifted 0.1 μm redwards.
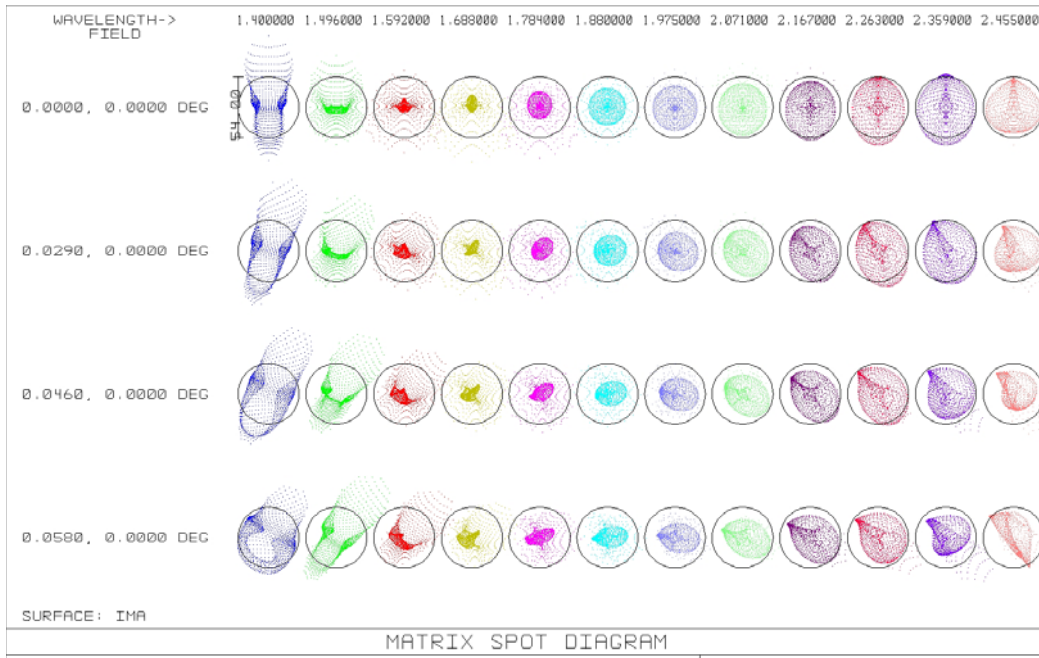
Figure 13.5-41. Same as for **Figure 13.5-39** except for red wavelengths.

13.5.10.4　　Spectroscopic Mode Image Quality Tables

```
Configuration:  1,    450 gpm

 Averaged over all wavelengths and field angles with refocus 29.307 mm

            rms    80%    90%    95%  diameters (microns)
           19.3   20.2   30.5   38.7

        X Field angles (arcmin):
                   0.0000   1.7400    2.7600    3.4800
        Y Field angles (arcmin):
                   0.0000   0.0000    0.0000    0.0000

        RMS Image Diameters:
           1.00000     29.1      29.1      30.1      34.4
           1.05300     20.9      20.4      20.7      23.2
           1.10500     14.0      13.3      13.8      15.1
           1.15800     17.1      14.5      12.3      12.4
           1.21000     19.7      18.4      15.9      14.4
           1.26300     20.1      20.1      18.6      17.0
           1.31500     21.3      21.2      19.5      18.0
           1.36800     22.8      21.3      18.9      17.7
           1.42000     21.3      19.1      17.3      17.3
           1.47300     17.9      17.1      17.0      18.3
           1.52500     17.6      17.3      19.0      22.6
           1.57800     18.9      20.3      20.9      18.1


        80% Encircled Energy Diameters:
           1.00000     35.1      35.4      33.8      41.0
           1.05300     25.4      25.0      25.6      26.9
           1.10500     17.0      16.8      17.0      17.6
           1.15800     16.1      15.4      14.2      15.0
           1.21000     16.2      15.5      15.8      15.6
           1.26300     15.0      15.2      15.6      16.5
           1.31500     16.0      16.1      16.6      17.2
           1.36800     19.8      18.5      17.4      18.1
           1.42000     19.6      19.7      17.9      18.6
           1.47300     20.8      20.0      18.4      18.9
           1.52500     21.5      19.5      18.8      23.5
           1.57800     20.9      22.1      22.9      21.5
```

```
Configuration:  2,    450 gpm

Averaged over all wavelengths and field angles with refocus 29.329 mm

              rms     80%     90%     95%  diameters (microns)
              25.2    27.8    41.2    50.3

        X Field angles (arcmin):
                    0.0000    1.7400    2.7600    3.4800
        Y Field angles (arcmin):
                    0.0000    0.0000    0.0000    0.0000

        RMS Image Diameters:
            0.90000      54.1      52.5      52.4      58.1
            0.95200      38.1      37.5      36.4      36.0
            1.00400      21.4      21.9      23.1      24.0
            1.05700      16.1      13.8      12.9      14.3
            1.10900      17.7      16.4      13.9      12.7
            1.16100      19.4      20.0      18.5      16.6
            1.21300      22.7      23.2      21.7      19.8
            1.26500      25.9      25.0      22.7      21.0
            1.31700      25.3      23.4      21.5      21.4
            1.37000      20.3      19.8      20.9      24.0
            1.42200      17.4      20.1      25.9      31.8
            1.47400      23.9      28.2      30.2      24.5


        80% Encircled Energy Diameters:
            0.90000      69.3      69.3      69.7      77.5
            0.95200      47.0      48.3      47.4      43.3
            1.00400      27.9      28.1      29.9      30.2
            1.05700      18.0      16.2      15.5      16.9
            1.10900      15.3      15.0      15.2      15.0
            1.16100      16.0      14.2      14.1      14.5
            1.21300      19.6      20.0      21.0      19.5
            1.26500      23.2      24.6      23.4      21.9
            1.31700      23.8      25.5      22.3      21.2
            1.37000      18.1      19.4      19.9      22.7
            1.42200      16.4      18.2      25.6      36.0
            1.47400      23.3      31.1      35.4      30.7
```

```
Configuration:  3,    255 gpm

Averaged over all wavelengths and field angles with refocus 29.394 mm

                rms    80%    90%    95%  diameters (microns)
               32.1   37.9   47.2   54.2

        X Field angles (arcmin):
                    0.0000    1.7400    2.7600    3.4800
        Y Field angles (arcmin):
                    0.0000    0.0000    0.0000    0.0000

        RMS Image Diameters:
            1.40000    42.5    47.9    51.5    45.4
            1.49600    27.9    30.7    36.7    43.2
            1.59200    26.1    25.6    26.4    28.7
            1.68800    26.4    24.9    23.6    23.7
            1.78400    26.0    24.4    22.8    22.6
            1.88000    27.3    25.2    23.4    23.4
            1.97500    30.6    27.8    25.7    25.9
            2.07100    33.7    31.0    29.4    30.1
            2.16700    36.3    34.8    34.4    34.5
            2.26300    40.5    39.8    38.4    36.0
            2.35900    43.8    40.9    35.8    31.3
            2.45500    37.3    33.0    29.2    34.5


        80% Encircled Energy Diameters:
            1.40000    50.9    59.8    62.8    53.2
            1.49600    33.1    35.1    40.8    53.0
            1.59200    27.0    28.1    28.9    30.3
            1.68800    21.8    22.8    23.4    24.8
            1.78400    24.6    24.2    24.5    24.3
            1.88000    31.6    30.4    28.0    28.6
            1.97500    38.0    33.8    31.3    30.7
            2.07100    42.1    38.1    35.0    35.8
            2.16700    44.4    42.0    42.4    43.3
            2.26300    50.3    49.8    48.4    45.5
            2.35900    53.2    51.4    44.8    38.7
            2.45500    45.8    40.7    36.2    44.2
```

The performance between 1.0 and 2.5 μm is quite good, but begins to suffer below 0.95 μm if the spectrograph is focused over a broad spectral region. At 0.9 μm, the 80% encircled energy diameter is 0.29″ at full field.   When the optics are focused to cover the J and H bands (1 to 1.8 μm), the worst 80% encircled energy diameters are just over 0.15″. When the optics are focused to cover the H and K bands, the worst 80% encircled energy diameters are 0.23″, with almost all below 0.20″. For reference 18 μm at the detector corresponds to 0.067″.

13.5.11   Appendix C: Grating Efficiencies
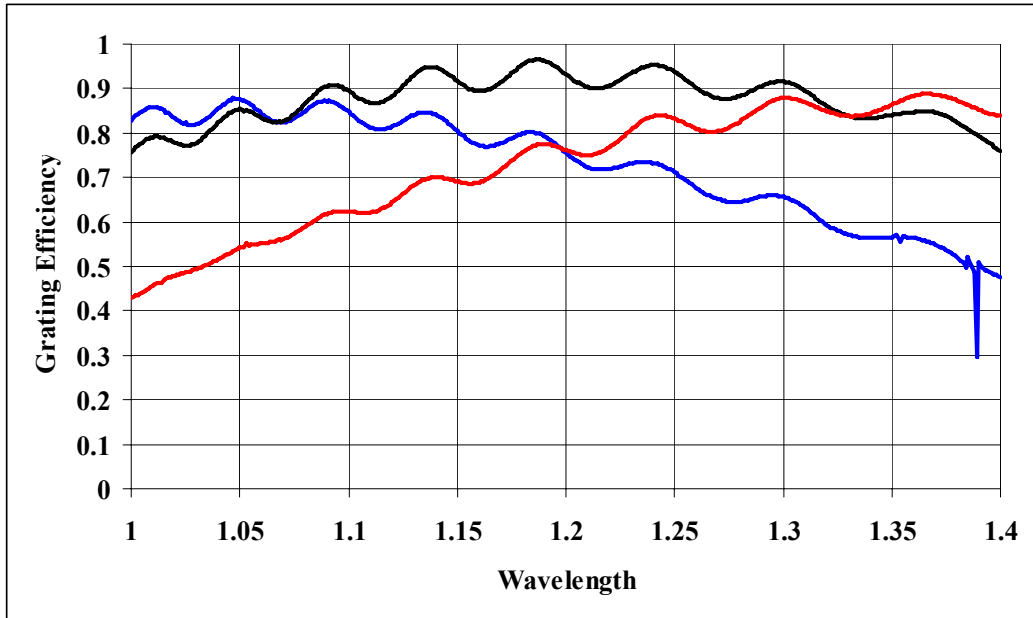
Figure 13.5-42.   J-Band 450 lpm VPH grating offering R=2825. The nominal index is 1.3, index modulation is 0.060, thickness is 10.0 μm, 45º polarization.   The black curve shows the efficiency for light incident on-axis in the dispersion direction with a Bragg angle of 15.66º (in air). The red and blue curves show the efficiency for light incident off-axis in the dispersion direction, corresponding to angles of ±2.5′ at the telescope focus.
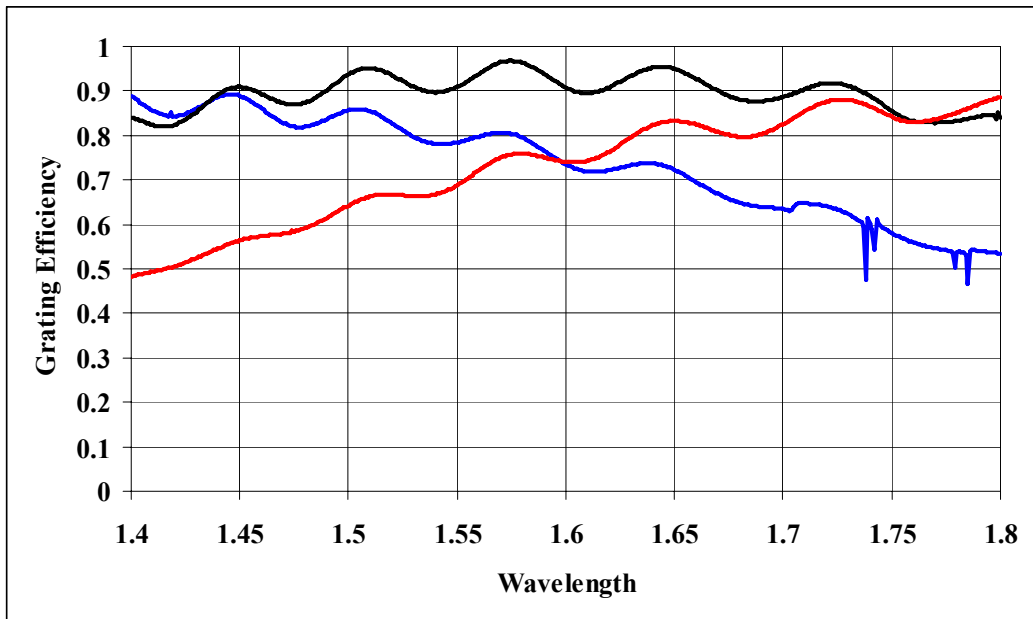

Figure 13.5-43. H-Band 360 lpm VPH grating offering R=3000. The nominal index is 1.3, index modulation is 0.060, thickness is 13.3 μm, 45º polarization.   The black curve shows the efficiency for light incident on-axis in the dispersion direction with a Bragg angle of 16.74º (in air). The red and blue curves show the efficiency for light incident off-axis in the dispersion direction, corresponding to angles of ±2.5′ at the telescope focus.
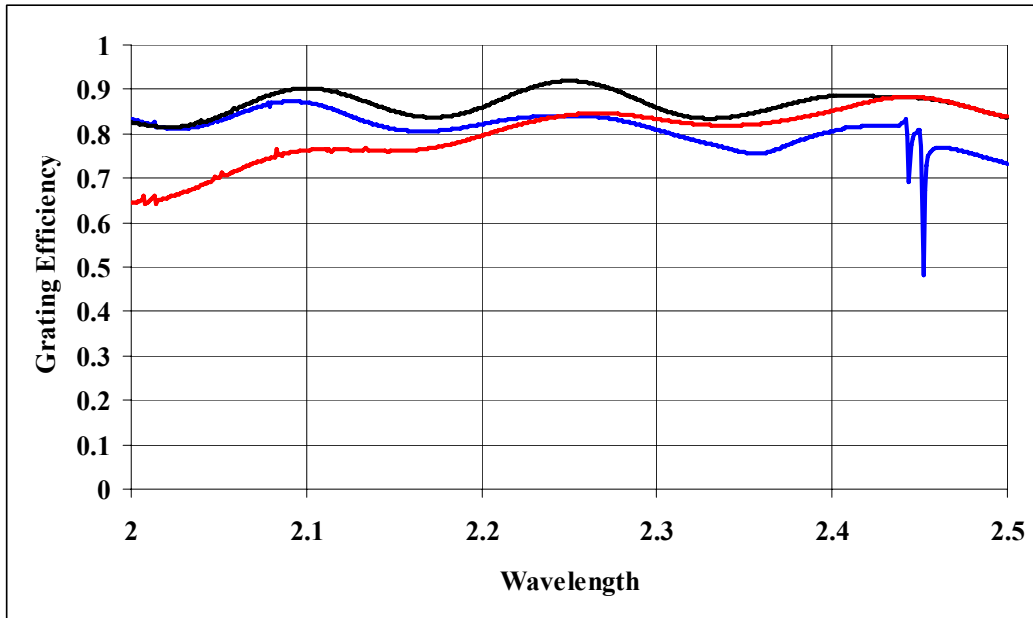
Figure 13.5-44. K-Band 255 lpm VPH grating offering R=3000. The nominal index is 1.3, index modulation is 0.1.05, thickness is 11.0 μm, 45° polarization. The black curve shows the efficiency for light incident on-axis in the dispersion direction with a Bragg angle of 16.67° (in air). The red and blue curves show the efficiency for light incident off-axis in the dispersion direction, corresponding to angles of ±2.5′ at the telescope focus.
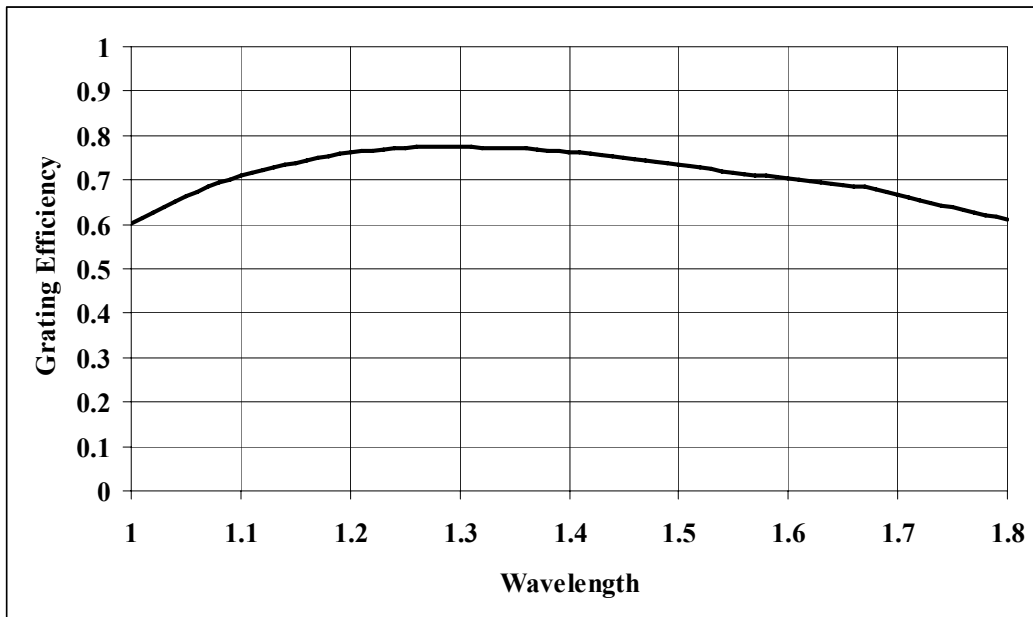
Figure 13.5-45. JH band grism offering R=1400. This surface relief grating has 175 lpm and a blaze angle of 28.2°.
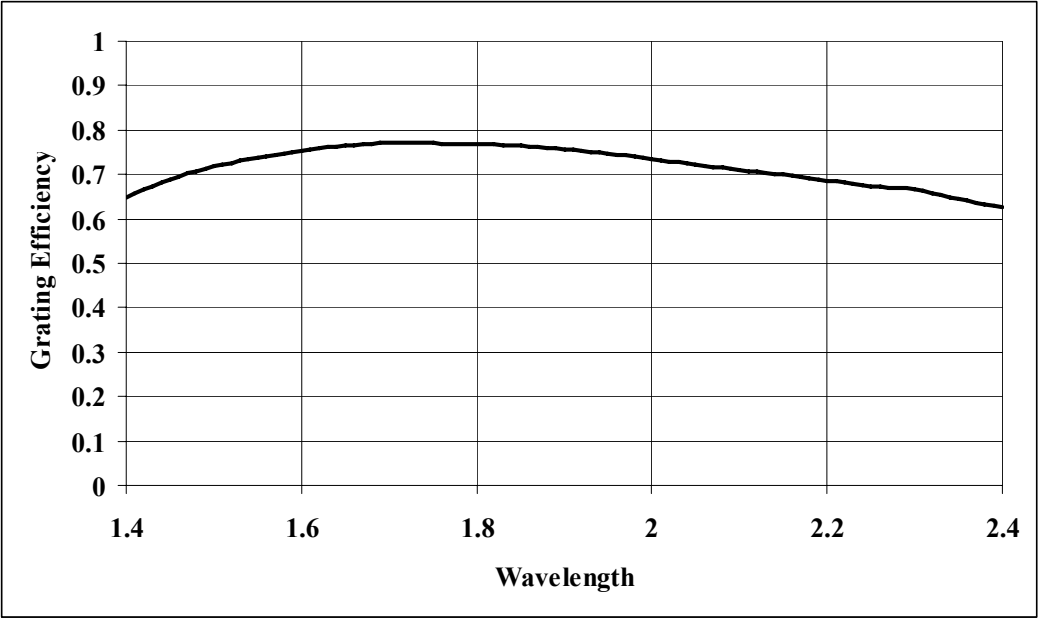
Figure 13.5-46. HK band grism offering R=1400. This surface relief grating has 130 lpm and a blaze angle of 29.6º.